Environmental Chamber to Regulate Film Morphology for Solar Energy Materials Printing Using Additive Manufacturing and Investigating the Role of Additives in Perovskites

Karthik Unnikrishnan

A thesis

submitted in partial fulfillment of the

requirements for the degree of

Master of Science in Mechanical Engineering

University of Washington

2018

Committee:

J. Devin MacKenzie

Vipin Kumar

Corie L. Cobb

Program Authorized to Offer Degree:

Mechanical Engineering

University of Washington

Abstract

Environmental Chamber to Regulate Film Morphology for Solar Energy Materials Printing Using Additive Manufacturing and Investigating the Role of Additives in Perovskites

Karthik Unnikrishnan

Chair of the Supervisory Committee:

J. Devin MacKenzie

Department of Materials Science & Engineering and Mechanical Engineering

Flexible ink solar cells are gaining increased interest from photovoltaic researchers and the rapid development in the field of additive manufacturing has made the fabrication of solution-processed hybrid organic-inorganic metal halides viable. The aim of this work is to assist the transition from lab-scale spin-coated solar cell active layer processes that cannot be effectively scaled up to a viable slot-die coat additive manufacturing process with the ultimate aim of transferring to an integrated roll-to-roll process. This thesis presents work done in solution engineering, establishing print parameters for the slot-die coater, introducing a processing step and hardware improvement to control and improve printed active layers and investigating the use of additives in perovskite precursor solutions. The perovskite precursor solution was developed based on experiments conducted on a large area flat sheet coater in ambient and a humidity-controlled room at the Washington Clean Energy Testbeds (WCET). Film deposition

experiments were followed by microscopy, spectroscopy and absorbance studies on the printed films. Based on visual observation and morphology data, the print parameters and solution composition are then altered. A local atmosphere processing improvement and hardware were introduced during solution printing and the effect on the perovskite microstructure including but not limited to grain morphology, grain boundary, grain size and film roughness was analyzed. An environmental chamber incorporating an air-knife was designed, fabricated and implemented in the deposition process that makes use of a recirculation zone created by constrained nitrogen to control and improve printed films. A contour of the airflow pattern was simulated on ANSYS 18.1, giving us a visual representation and quantitative estimations of the air flow over the printed film. Through experiments, it was possible to regulate the microstructure based on the evaporation rate induced by the recirculation zone. The chamber also played a role in keeping oxygen and moisture away from the print zone, thereby offsetting issues caused by a highly hygroscopic Methylammonium Iodide (MAI). A preliminary study was done with a prototype chamber after which a large-area final chamber was built. A study on additive inclusion in perovskites was done that made use of high boiling point antisolvents to regulate crystallization dynamics. The additive concentrations were varied with respect to annealing times and printing trials were performed from these inks on the slot-die coater and compared to arrive at a desirable precursor perovskite solution composition.

Acknowledgements

I would like to express my appreciation to my advisor Professor John Devin Mackenzie and my committee members, Professor Corie L. Cobb and Professor Vipin Kumar for their continued support and for attending my defense presentation. I owe thanks to my advisor for presenting me with the opportunity to conduct research at the state of the art open access facility, the Washington Clean Energy Testbeds. Access to research equipment like the slot-die coater and other analysis equipment was convenient due to the continued support, expertise and training from Dr. Felippe Pavinatto and Dr. Phillip A. Cox.

I am especially grateful to Brandon T. Rotondo without which the completion of my research would not be possible. I extend my thanks to him for assisting me in conducting experiments and introducing me to material science concepts. His help throughout the course of the project during fabrication and formulating the hypothesis contributed to a successful completion of the project.

I also extend my sincere thanks to the Material Science and Engineering department for assisting me in manufacturing components for my project and for access to the Abrasive Water-jet Cutter. I also thank the Mechanical Engineering department in supporting me by providing access to the workshop facilities.

In addition, I appreciate all collaboration and ideas from my lab colleagues. Finally, and most importantly, my furthermost appreciation goes towards my family and friends for offering their priceless love and help at every moment throughout my master's program.

Table of contents

List of tables

List of figures

1. Introduction

Ever since man realized the sun's potential to harness energy using the photoelectric effect, engineers of the 20th century have directed their efforts to utilize the resource effectively. The change from $300 per watt to $2.49 per watt [1] for a solar panel highlights the evident amount of research and engineering that has gone into bringing this technology to the forefront. World energy consumption is rising at 28% between 2015[2] and 2040. Along with global warming due to industrial, commercial, residential and transportation [3] needs, we are gradually advancing to a point where our increasing energy consumption trends will cause a decline in the air quality and ultimately having a detrimental effect on our planet. Research in solar energy has made it possible to envision that our energy demands can be fulfilled by a renewable resource [4]. Currently, solar generation is the fastest-growing electricity source, which is expected to reach about 36% of total U.S. renewable generation by 2050. Solar installations in the USA have reached an estimated installed capacity of 30 GW along with a 50% reduction in the cost of a solar electric system over last 5 years [5].

On a global scale, India has invested in solar power, utilizing their solar resource with about 20 GW of installed capacity, expanding their generation capacity by 8 times since 2014[6]. China leads the solar energy market, slightly ahead of Germany with about 78GW of installed capacity for both solar thermal energy and photovoltaics [6]. Following China, German solar power accounts for about more than 6% of the country's electrical generation and has an installed capacity of 41GW [7]. Direct solar to electricity conversion relies on the use of the semiconductor technology coming to be known as Photovoltaics. Photovoltaic (PV) energy systems are poised to play an increasingly important role in global power generation. Since 2003, the share of global energy generation derived from photovoltaics has grown at an average rate of 49%/year [8]. The International Energy Agency (IEA) anticipates this exponential growth to continue. The IEA estimates that the global share of energy generation from PV systems will reach 16% by the year 2050.

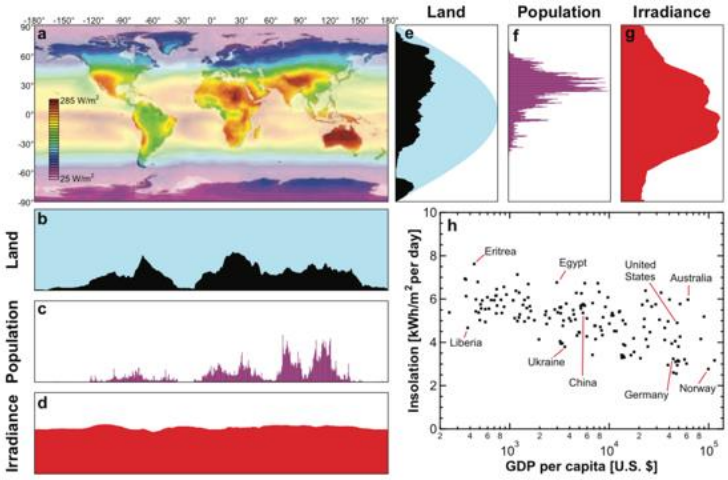

Figure 1 A comparison between the solar resource, land resource and population along with insolation vs world GDP [9](Reproduced from Ref. 9 with permission from Bill Rankin, Associate Professor, Yale University)

1.2 Method of using the solar resource

Light is converted to electricity in a photovoltaic cell when photons emitted from the sun penetrate and are absorbed in a photoactive semiconductor material and the resulting excited state is acted on by potential gradients in the cell, releasing mobile electron and hole charge carriers that travel to corresponding collection terminals with different potentials. Electrons and hole-derived currents can be conducted from these cell terminals through an external circuit and do work corresponding to the potential difference between the charge carriers at the cell terminals. This is the photoelectric effect that was observed in 1839[10] by Edmond Becquerel. The first semiconductor solar cell was a Selenium solar cell built by Charles Fritts in 1883, followed by a 6% efficient solar cell with a p-n junction. Crystalline silicon came into the picture as a solar cell active material in the 1950's, a major development in the solar energy industry. The abundance of silicon and emerging manufacturing technologies to fabricate silicon solar cells derived from the growing silicon electronics industry made the solar energy industry a promising sector. Today, the solar to electrical power conversion efficiency (PCE) of single crystalline silicon solar cells has reached a record efficiency of 27% [11]. Multijunction solar cells made of several semiconductor materials have been developed with efficiencies as high as 46% and efficiencies are still increasing. To date, however, the additional costs associated with

processing multijunction cells has prevented them from being widely adopted. Emerging solar cell technologies including thin films which could be made at lower cost and with lower invested energy [12] have reached up to promising efficiencies of 22.3% making it an interesting domain for research. The advent of solution processed solar cells like organic solar cells, perovskites and quantum dots have the added benefit of rapid production, low carbon footprint manufacturing and low capital, manufacturing and material costs. Solution formulation of different precursors allows for easy band gap tuning to increase the range of solar light spectrum wavelengths that can be absorbed. The different types of photovoltaic technologies being employed have grown exponentially. Research has been focused on various emerging high efficiency materials, layer structures and manufacturing techniques.

1.3 Types of photovoltaic solar cells

Photovoltaics can be broadly classified by the substrate on which the active layer is based on. A commonly used type of solar cell is the *wafer-based cell*. These cells rely on panel encapsulation, mechanical supports and fixtures to be installed for use and usually tend to be bulky. Thin film photovoltaics represent a category of solar cells that can be integrated into panels during the cell formation process without additional assembly that are categorized by a thin active layer, lower cost, inactive substrates, reducing manufacturing, and material wastage [13].

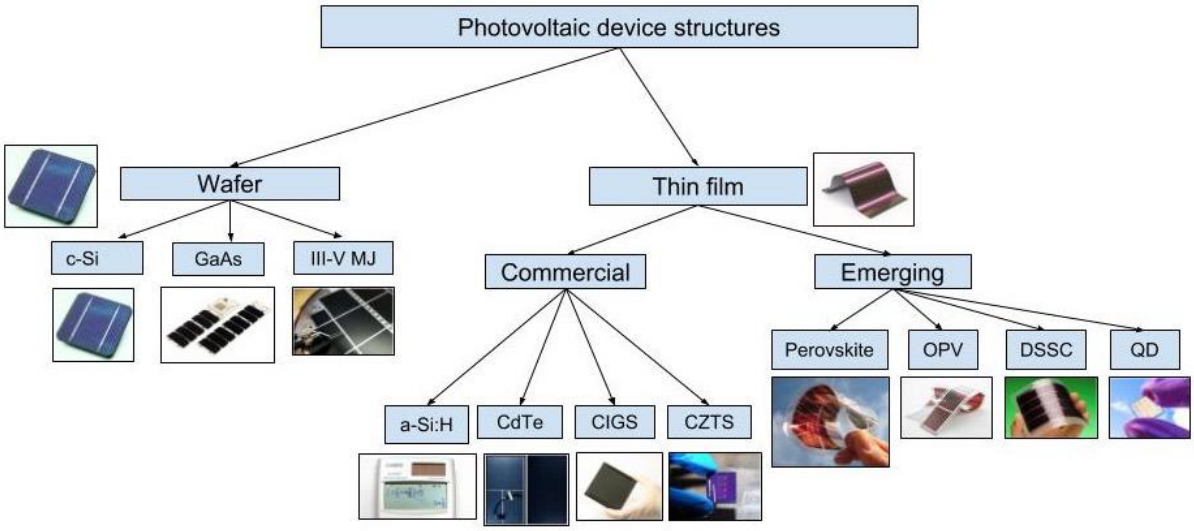

Figure 2 Classification of types of PV systems

Wafer based:

Silicon (c-Si): These solar cells constitutes more than 90% of the global module production. Crystalline silicon solar cells are further classified into *single crystalline (c-Si)* and *multicrystalline (mc-Si or polysilicon)*. Single crystalline solar cells are typically fabricated from large single crystal boules in the *Czochralski* (CZ) process, whereas block casting from liquid silicon produces randomly oriented crystalline grains to be used in multicrystalline cells. To accommodate for their weak light absorption properties, thick silicon wafers of the order of 100 µm have to be used [13].

Gallium Arsenide (GaAs): This compound of Gallium and Arsenic is a semiconductor material having a direct bandgap with strong absorption properties that is well matched to efficiently harvest photonic energy from the solar spectrum. GaAs has achieved efficiencies of close to 28.8% for single-junction lab grade cells [13]. Gallium Arsenide poses several other benefits over silicon cells in terms of thinner active layer requirements, lower temperature coefficient, good low light performance, higher efficiencies and lighter weight [14].

Multijunction solar cells (III-V): These devices use multiple bandgaps and junctions which are tuned to efficiently harvest a broader range of the solar spectrum with record efficiencies of 46%. These devices find use in small-scale applications and are currently limited to the aerospace industry owing to its high cost but lightweight power generation metrics [17]. Typical multi-junction cells use multiple absorbing sub-cells that extract more energy out of multiple regions of the solar spectrum pushing the theoretical maximum efficiency with increase in the number of junctions. Multijunction cells have not been feasible on a terrestrial scale, except in some concentrator systems that use less cell area per unit solar collection area, owing to the high manufacturing and materials costs involved[13].

Thin-film:

Thin film solar cells account for approximately 10% of the PV market and represent a promising growth area due to their low cost, fast manufacturing speeds, and lesser material requirements [8]. Thin film solar cells have an active layer, typically microns in thickness or less, that is thinner than the human hair, making it more flexible and reducing materials costs and the associated embedded energy of thick semiconductor cell substrates. This property also allows it to be used without the need for extensive mechanical supports and fixtures. Extensive research into thin-films have made it possible to use cheap printing methods, easing the transition from lab to commercial scale.

Hydrogenated amorphous silicon (a-Si:H): This is a non-crystalline, thin film form of silicon that offers stronger absorption than crystalline silicon and lower production costs. These cells possess larger bandgaps — at 1.5–1.8 electron volts (eV) compared to 1.12 eV for c-Si — which reduces the range of wavelengths that can be absorbed [13] and efficiencies have trailed behind other approaches.

Cadmium telluride (CdTe): These cells have a record efficiency of 22.1% and are the most efficient and cheapest solar cell technology as of today [13]. These particular solar cells were developed by FirstSolar. A p-doped CdTe layer matched with an n-doped cadmium sulfide (CdS) acting as a window layer, forms the part of a simple p-n heterojunction structure. It

is structurally similar to the heterojunction in CIGS cells. As with most thin-film solar technologies, carrier collection is accomplished by drift, or field-assisted collection [18].

Copper indium gallium diselenide ($CuIn_xGa_{1-x}Se_2$, or CIGS): One of the most interesting and controversial materials in solar energy is Copper-Indium-Gallium-Selenide. It is a demonstrably capable and versatile material. Even though a-Si and CdTe (the other thin-film technologies) have continually improved their efficiency, CIGS has improved and maintained a distinct advantage because of their higher efficiency and flexible substrates. The major disadvantage is that, the versatility of these cells makes its behaviors unexplored and limits the understanding of grain boundaries. Material defects also leads to a low open circuit voltage [19].

Copper zinc tin sulfide (Cu_2ZnSnS_4, or CZTS): The semiconducting compound (CZTS) is made up of earth-abundant, low-cost and non-toxic elements, making it an ideal candidate to replace other types of solar cells that face material scarcity and toxicity issues [20]. The device performance of CZTS-based thin film solar cells has steadily improved over the past 20 years, reaching near commercial efficiency levels (10%). These achievements prove that CZTS-based solar cells have the potential to be used for large-scale deployment of photovoltaics [20].

Dye-sensitized solar cell (DSSC): Dye-sensitized solar cells generate energy through the movement of the electrons to and from the dye. The dye produces electricity once it is sensitized by incoming light. It behaves like chlorophyll in plants by absorbing the photons from the sunlight resulting in an excited electronic state. The dye injects the excited electrons into a semiconductor which is conducted away by nanorystalline titanium dioxide. The use of sensitizers having a broad absorption band in conjunction with oxide films of nanocrystalline morphology permits to harvest a large of sunlight [21].

Colloidal quantum dot photovoltaics (QD): In an attempt to replace bulk solar cell materials, *quantum dot technology* was introduced. These are three dimensionally confined

semiconductor nanostructures that represent a new class of functional materials for photovoltaic applications. The bandgaps of quantum dots can be tuned by changing the size of the dots in addition to gaining a degree of control for varying the composition, structure and shape. The quantum dots have a particle size smaller than the size of the Exciton Bohr radius and due to quantum mechanics considerations, the electron energies that can exist within them become finite, like energies in an atom [22]. Due to their small size, they can be dispersed into solvents and processed from solution at low temperatures.

Organic photovoltaics (OPV): This is one of the less toxic and cheaper alternatives to other thin-film technologies. It uses small semiconducting conjugated polymers or molecules to absorb light. Its photoactive layers consist of acceptor and donor layers, which absorb light and generate photocurrents. These layers absorb light to form neutral excitons, which are basically, bound electron-hole pairs that are excited into the conduction and valence bands. The current is generated when the electrons and holes are separated at the acceptor/donor interface and move to their respect electrodes [23]. OPV solar cells are an immature technology with a large number of variants still under development although efficiencies exceeding 10% have been achieved [24]. The amount of photocurrent generated is limited because of short charge carrier mobility and diffusion lengths negatively affecting its power conversion efficiencies [25].

Perovskite solar cells: *Hybrid organic/inorganic perovskites* are an emerging technology and still requires more research before being deployed in large-scale applications. These are considered one of the most promising technologies for future photovoltaics because of their unique structure and a variety of properties like a broad absorption spectrum, fast charge separation, high absorption coefficient, long carrier diffusion length and long carrier separation lifetime [26]. The availability of inexpensive perovskite precursors in the solution form enables low cost manufacturing techniques. One of the major challenges for this technology is the degradation of organic/inorganic trihalides to PbI_2 (Lead Iodide) in the presence of moisture and other impurities, affecting its stability [25].

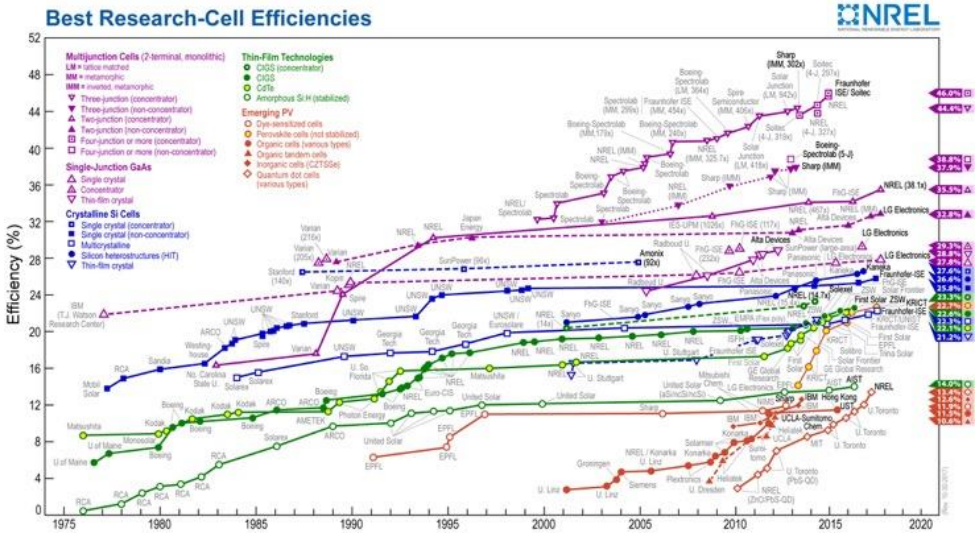

Figure 3 NREL Best research-cell efficiencies [11]

1.4 Working of a Photovoltaic cell

The small discrete quantum packets of light energy known as a *photon*, after it passes into the active layer of a solar cell, can excite an electron from its valence band state if it has an energy in excess of the band gap energy of the active layer semiconductor. In this case the electron takes on transferred energy from the photon and is promoted to the conduction band where it is a mobile carrier of negative charge. The excited electron leaves behind a vacant position in the valence band creating what is known as a *hole*. Holes in the valence band are also mobile states with a positive charge that can move through diffusion or under the influence of electric fields. The electrons and holes in the conduction band and valence band, respectively are collected at the respective terminals creating a potential difference. A load can be placed between the terminals, completing a circuit resulting in a photo induced current driven by the potential difference between the two terminals. A typical silicon solar cell produces voltage in the range of 0.5-0.6 V DC. The active area, irradiance and cell efficiency ultimately determines the current generated and power produced [26]. These photovoltaic cells are arranged together and electrically connected in series strings to build up high voltages and encapsulated to form a *module or panel*. These numerous panels can then be arranged in a desired manner with mechanical supports to form an *array*.

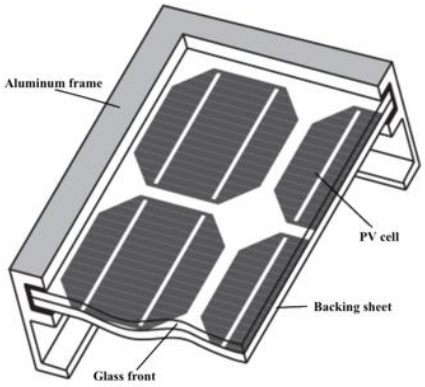

Figure 4 Schematic of a PV cell [27]

1.5 Solar cell physics

An n-type (electron dominant) silicon layer is formed adjacent to a p-type (hole dominant) material to form a semiconductor junction, which is typical for a semiconductor-based solar cell device architecture. The *depletion zone* is a region of high electric field around the p-n junction formed through electron diffusion from the n-type material into the p-type material and holes diffusing down the hole concentration gradient between the p- and n-type regions. The mobile photoexcited electrons and holes are driven to opposite faces of the solar cell by the electric field in the depletion region. Contacts to the different face of the cells which are attached to positive and negative terminals. A photon will only be able to excite an electron out of its bound valence state provided the energy of the photon is greater than the *band gap* of the material. Thus, the band gap plays a significant role in a photovoltaic device. The band gap is essentially defined as the difference between the valance band and the conduction band in a solid material and represents the threshold energy required to excite an electron into the conduction band[28]. The cell consists of donor and acceptor layers of entirely different materials. Few solution processed cells (OPVs) have a characteristic HOMO (highest occupied molecular orbital) and LUMO (Lowest unoccupied molecular orbital). Here, the band gap is referred to as the distance between the HOMO and the LUMO [29]. Photons that hit the donor or the acceptor create an exciton (electron-hole pair), which remains in a non-excited state. The excitons gain energy after

they travel to the interface between the donor and the acceptor layers. The efficiency of charge separation and ultimately quantum efficiency in an OPV is then determined by the probability of the exciton reaching an acceptor/donor interface before recombination occurs [30]. This probability is dictated by the exciton diffusion length, which is typically small in organic semiconductors. In solution processed solar cells, the active layer is sandwiched between a *hole transport layer* and an *electron transport layer*.

2. Literature review

Perovskites when deposited on to a substrate, result in a multicrystalline grain orientation that can be regulated by altering the processing parameters. A highly packed defect-free grain structure with narrow grain boundaries is desired to ensure high device performance. Giovanni et al. demonstrated the use of an air-knife in perovskite printing to control the temperature gradient and gain control over the crystallization dynamics. It was observed that a low substrate temperature affects the solvent evaporation rate affecting the crystal growth. Printing was done on a slot-die coater using a 40 wt % solution of Methyl ammonium iodide (MAI) and Lead Iodide ($PbCl_{2)}$ [3:1 molar ratio] in Dimethylformamide (DMF). A device performance of 9.2% was achieved with layers of reduced surface roughness [31]. Degradation mechanism in ambient air is explained in great detail, with a good insight into the formation of intermediate hydrate phases in ambient air by Masaki et al. This poses all the more reason to explore the influence of air-knife drying in ambient air aiming to achieve good control over the humidity [32]. The utilization of nitrogen during fabrication can help isolate the perovskite film from oxygen and moisture to create a localized low-humidity and oxygen zone over the deposited film [33]. Gangishetty et al. fabricated a perovskite device using a sequential deposition method by varying the RH% resulting in devices with 12.2% efficiency contrary to failed devices due to perovskite degradation as previously reported. It was found that the gaps between individual grains decreases with increasing humidity. A higher RH also promoted the formation of large densely packed grains with minimal grain boundaries showing that high humidity does not

necessarily deteriorate cell performance [34]. Gao et al. used a multi-flow N_2 arrangement with passes for air-inlet and outlet and successfully printed films with low surface roughness with high performance characteristics [35]. Evaporation mechanisms were explored with specific interest in solvent evaporation by bringing *gas thickness* into the picture which is a critical value that dictates the complete evaporation of the solvent. Although, it is unclear how the thickness value in collaboration with the N_2 airflow setup influenced their results, it presents a likely area of interest to be explored. The solvent evaporation rate plays a major role in the nucleation and growth of crystals and Bi et al. demonstrated this by using different coating temperatures to vary the evaporation rate [33].

Based on a few such papers and results from our preliminary analysis, we arrived at an initial composition of a perovskite precursor solution to proceed with N_2 flow studies. The N_2 flow system will be investigated with varying precursor solutions. For solution optimization studies, Yixin et al. explored the use of Methylammonium chloride (MACl) in controlling crystallization dynamics which had a beneficial effect on absorption of light by $CH_3NH_3PbI_3$ in addition to improved surface coverage of coated films on a planar substrate [36]. MACl concentrations were varied in perovskite precursors but when printed via a one-step sequential deposition by a slot-die coater, a major change in film quality was not observed. The use of an additive, 1-Chloronaphthalene (CN) in our precursor solution was based on work by Xin et al., when it was used to control the crystal growth formation and absorption profile due to its relatively high boiling point and steric effects caused by the aromatic naphthalene ring. It is shown that CN improves film morphology, beneficially affects the surface coverage and also shows improved light absorption which is verified by a high device efficiency. The CN additive concentrations were varied, and the films were characterized [37]. Our experiments performed within a temperature range of 70°C-110°C, confirm a perovskite conversion temperature of 95°C to give improved results, with the planar architecture on a metal oxide scaffold arrangement. The paper [31] draws on the hypothesis of control over the crystallization dynamics by means of temperature gradient between the substrate and ambient air from the air-knife. Instead we aim at exploring the crystallization dynamics with respect to grain sizes, grain boundaries and smoothness of the printed layer as influenced by solvent

evaporation with aim to control it through a recirculation air-flow pattern created by a 12" air-knife. A Computational Flow Dynamics (CFD) analysis is also done to visualize the airflow pattern within the recirculation chamber. Cotella et al. achieved results by keeping the air-knife 20 cm away from the coating head and 25 cm above the substrate [31]. A large distance in the y-direction can lead to turbulence at the bed surface, affecting the drying. In this project, the air knife would be mounted 4 cm above the flat bed as shown in Fig. 7. The article published on degradation mechanisms of $CH_3NH_3PbI_3$ poses all the more reason to explore the influence of air-knife drying in ambient air by hoping to achieve a good control over the humidity by conducting experiments in an environmental control room at the WCET to iterate between N_2 drying and humidity parameters [38]. In comparison to researchers using non-scalable processes like spin-coating with devices of active area $0.0708cm^2$, our research project focuses on films with an active area 13 cm^2 [35].

3. Perovskites

Perovskites are unique materials with a general chemical formula ABX_3 in a structure akin to $CaTiO_3$, where the bigger cation is A and the intermediate sized cation is B, with the only anion being the X ion [39].

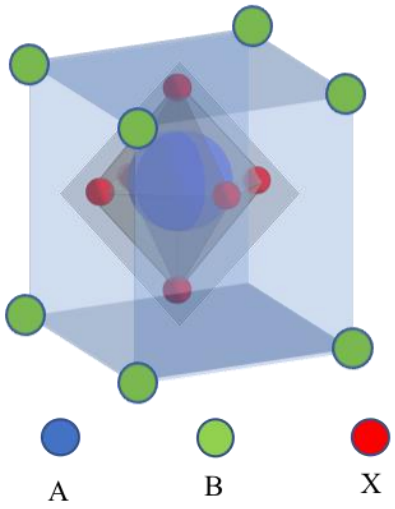

Figure 5 ABX_3 structure

In our lab-based applications, the perovskite composition typically used are organo-metal halide perovskites with the formula $CH_3NH_3PbI_{3-x}$ (Methyl ammonium Lead Iodides) where the X is replaced by monovalent halide anions (Cl^{1-}, Br^{-1}, F^{-1}, I^{-1}) and A and B sites are occupied by organic cations (Methyl ammonium (MA), Formamidinium (FA)) [40] and a divalent metal cation (Pb^{2+}, SN_2^{+}). For charge neutrality to be maintained in the ionic perovskite structure, the charges on A and B ions must be equal to the negative of thrice the charge on the X ion [39].

$$q_A + q_B = -3q_x \quad (1)$$

3.1 The properties of perovskites

The inherent flexibility of replacing the A, B and X sites with any alternate element to modify its physical and chemical properties is one of the reasons for its significance in material science [39]. The perovskite structure displays a variety of optoelectronic properties. Apart from being an interesting replacement for silicon for use in photovoltaics, it is also being investigated for use in LED's, piezoelectrics and dielectrics because of pyroelectricity, colossal magnetoresistivity and high temperature superconductivity [40]. Perovskites can work as n and p diodes because of its ambipolar nature [40], due to its balanced charge transport properties. The promising 1.55 eV bandgap of $MAPbI_3$ which can be tuned by changing the ions to fall in the 1.5-2.3 eV range makes it almost ideal for fabricating single-junction perovskite solar cells [41] as this band gap energy is close to the optimum for extracting energy from the solar spectrum which has a black body-like irradiance spectrum vs photon energy. Photoluminescence response studies indicate that long carrier lifetimes and diffusion length of an exciton (1 μm) reduces the chance of recombination allowing an open-circuit voltage of greater than 1V [42], [43].

Methyl ammonium trihalogenoplumbates (II) ($CH_3NH_3PbI_3$) have a perovskite crystal structure and upon heating, transitions to different structural phases. At the highest temperature, the crystals have a cubic symmetry which transforms to a tetragonal phase when the temperature decreases to 330 K and further reduction in temperature to 161 K would result in an orthorhombic structure [44]. These structural changes due to the ordering of ion positions are followed by a change in its lattice parameter. This change depends on the anion-cation bond lengths and thus only when the ratio of the A-X and B-X bond lengths equals √2, the ideal perovskite structure is established. This proposed relationship by Goldschmidt can be used to predict the formation of a perovskite phase. Thus, an ideal perovskite structure would be satisfied by the following relationship [39]:

$$\frac{r_A + r_B}{r_B + r_X} = \sqrt{2} \quad (2)$$

where r_A, r_B and r_X are the radii of the two cation sites A and B and the radius of the X site.

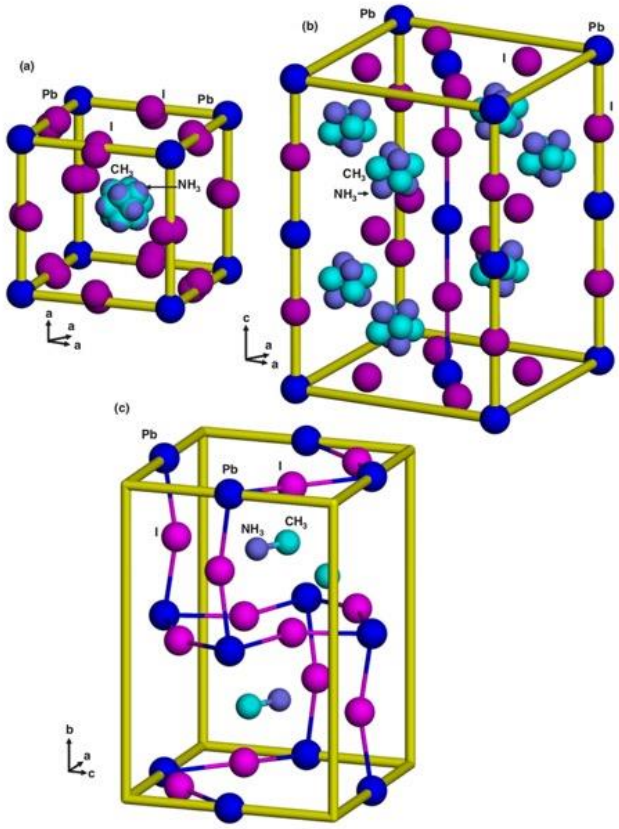

Figure 6 Transition structures of MAPbI3 a) cubic b) tetragonal c) orthorhombic (Image reproduced from Ref. 39 under the creative commons licence: https://creativecommons.org/licenses/by-nc-nd/4.0/) [39]

3.2 Solar cells

Perovskite solar cells are an emerging technology adapted from a DSSC (Dye Sensitized Solar Cells) cell architecture which had efficiencies of 3% when the first device was fabricated that has acquired attention in the solar cell research community. They are formed of intermediate layers between which the photoactive light absorbing layer is sandwiched. On absorbing light, electrons and holes migrate through the Hole Transport Layer (HTL) and the Electron Transport Layer (ETL) and are collected by the respective anodes and cathodes. The HTL's and ETL's favored are required to possess optical clarity, good electrical properties in addition to a stable chemical structure [45]. Typically, a perovskite cell structure is arranged as TCO/HTL/Active layer/ETL/Metal contact and can

be printed from top to bottom as desired.

Conductive polymers like polystyrene sulfonate (PEDOT: PSS) and Phenyl-C61-butyric acid methyl ester (PCBM) have been used as HTL's and ETL's for our application. The use of metal oxide nanoparticles as an HTL has also been explored. Transparent metal oxides have a wide band gap and are stable in air in addition to high conductivity partly due to a high free electron concentration [45]. Cathodes and anodes like (Ag, Al, Au and ITO) are typically vacuum deposited above and below the active layers of the cell based on the cell configuration. Many perovskite solar cell architectures have been experimented with by replacing these layers. For example, Bert et al. used an ITO/TiO_2/ $MAPbI_3$/P3HT/Au arrangement, Getachew et al. used an ITO/ZnO/$MAPbI_3$−IPA100/spiro-OMeTAD/Ag arrangement and Fukashi et al. used ITO/PEDOT:PSS/ $MAPbI_3$/ PCBM/ 1,3-Benzodioxol-5-yl(piperidin-1-yl)methanone (BCP)/Al.

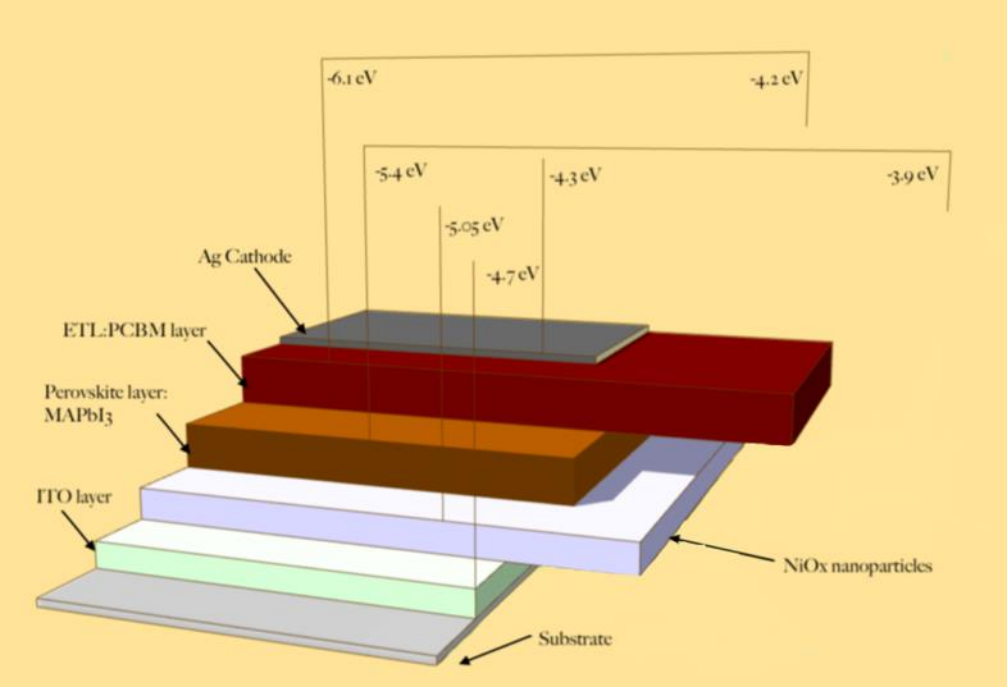

Figure 7 The structure of a planar perovskite solar cell with an inverted p-i-n architecture

3.3 Lab scale PSC parameters

Perovskite solar cells were introduced less than a decade ago, yet they have shown promising performance results with power conversion efficiencies comparable to conventional silicon solar cells. This performance and the relatively inexpensive manufacturing and material costs for perovskites have encouraged research in this field. Solution-processed solar cell researchers have scaled up from spin-coating to slot-die coating with an increase in the processible area and precursor materials utilization.

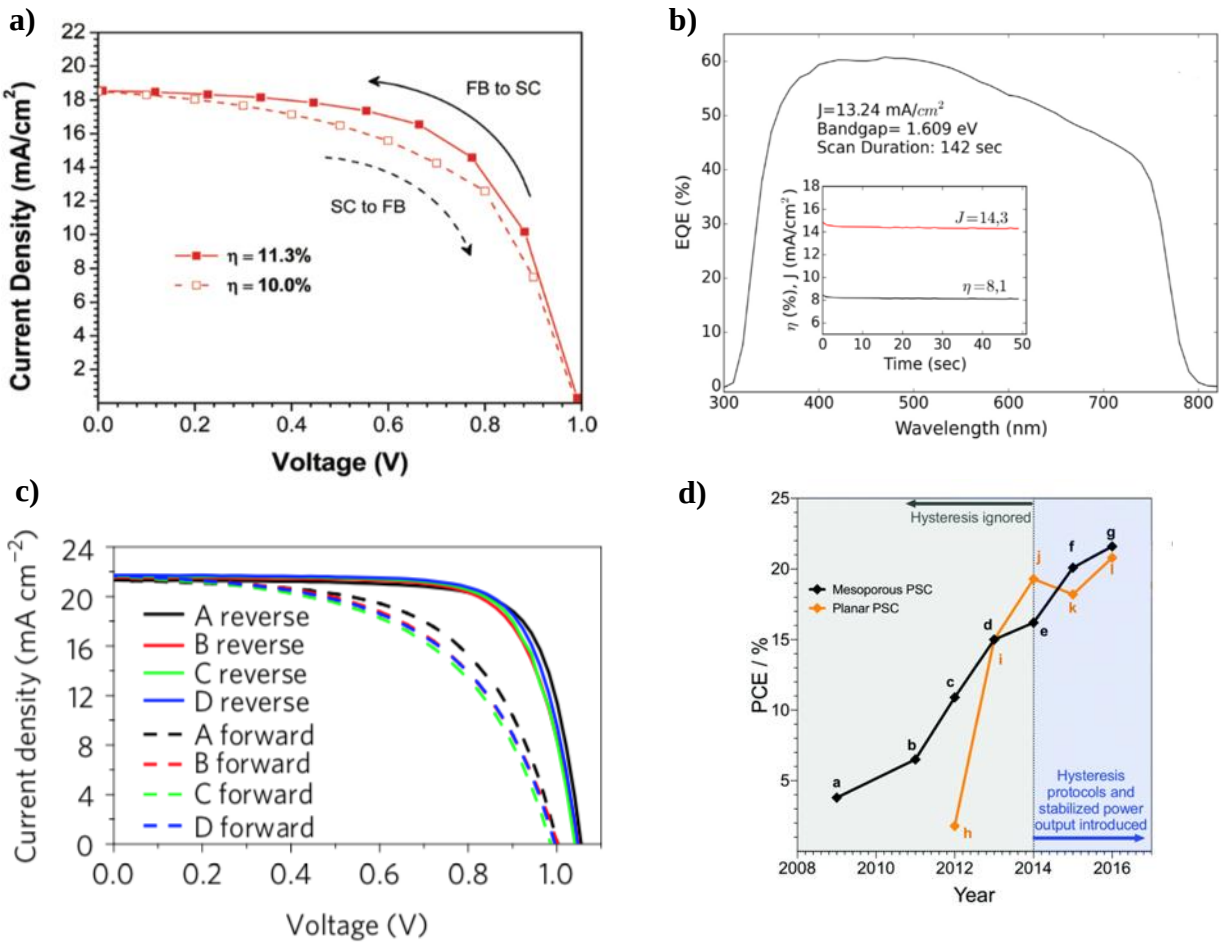

Figure 8 a) J-V curve of a Slot die coated cell [34](Reproduced from Ref. 34 with permission from the Royal Society of Chemistry]; b) External quantum efficiency measurement of a slot die coated cell [31] (Reproduced from Ref. 31 with permission from Elsevier); c) J-V curve of blade coated cells [46] (Reproduced from Ref. 46 with permission from nature energy); d) Progress in perovskite solar cell efficiency over the years: [47].

Mobility is defined as the ease with which charge carriers in a material travel when driven by an electric field. As electrical conductivity and conversely, parasitic resistive power losses, depend on the product of mobility and carrier concentration, these parameters are of immense significance. The charge carrier diffusion length is defined as the distance the carriers move before they recombine, which is a strong factor of the mobility and this has important implications on the dimensions of the active layers of the solar cell. In perovskites, a high electron mobility of the order of 0.06-1 cm^2/Vs and greater for its variants supports high performance metrics [48]. Long range diffusion lengths and charge accumulation also makes this a promising material for solar energy applications.

3.4 Benefits of perovskite solar cells

These benefits include the benefits that come from using thin-film flexible solution processed methods for fabricating solar cells.

- Employing inexpensive and roll-to-roll compatible methods like slot-die coating, screen printing, and flexographic printing will play a role in plummeting manufacturing and installation costs for photovoltaics.
- A tunable band-gap implies the use of additives and additional processing parameters to be easily introduced to obtain defect-free, pinhole-free and efficient solar cells.
- The ability to utilize flexible lightweight substrates to fabricate perovskite solar cells increases its range of applications by eliminating the use of mechanical supports and structures
- A broad absorption range in the electromagnetic spectrum and lab-scale efficiencies of over 22% [49] have already been achieved in a span of few years, whereas silicon solar cells took 60 years of development to match with similar efficiency values [12].

3.5 Commercial status for PSCs

Several companies [50] have research interests driven towards commercialization of PSCs. These developers are working on integrating the technology with currently available products to expand its applications and increasing the stability of the product

Oxford photovoltaics (https://www.oxfordpv.com)	United Kingdom
Saule Technologies (https://sauletech.com)	Poland
Great cell Solar (http://www.greatcellsolar.com)	Australia
Frontier Energy Solutions (http://www.frontierenergysolution.com)	South Korea
Microquanta Semiconductor (http://www.microquanta.com)	China
Solar-Tectic (http://www.solartecticllc.com)	United States

Table 1 Perovskite companies breaking into the commercial market.

4. Solar cell fabrication

4.1 Conventional Silicon to Solution processed solar cells

Unlike the high energy intensive processes, cost and material wastage inherent to the manufacturing of silicon solar cells, where a huge pool of metal is melted and recast in form of massive ingots, the fabrication of emerging third generation solar cells such as PSCs is a rather simple, cheap and an efficient process. That being said, solution processing methods involves dealing with complex issues such as optimal printing parameters, film quality and a homogeneous microstructure that ensures efficient charge transport. Solution

processing methods have also proved to result in films with high coverage of densely packed crystalline grains. This is validated by better lifetimes and electrical performance of PSCs using PL measurements [42].

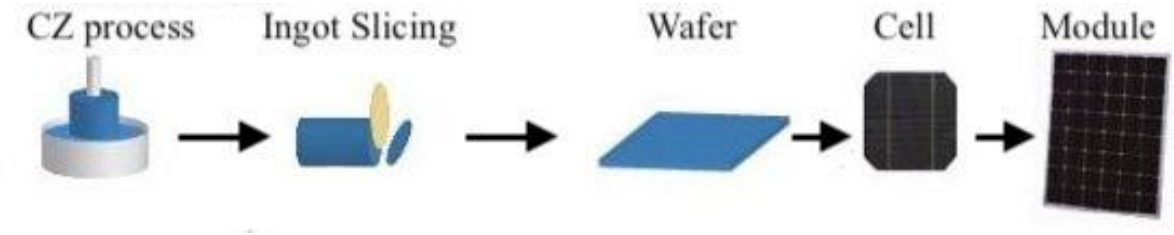

Figure 9 Silicon solar cell fabrication process

Figure 10 A silicon ingot of area 0.3-0.4 m^2 [51] weighing about 300 kg [52]

4.2 Spin coating

Lab scale perovskite solar cells are conventionally fabricated using spin coating. Precursor and solvent solution is dispensed onto a substrate, typically 1cm^2 in area. The substrate is then rotated at high speeds of up to 10,000 rpm. This high-speed rotation creates a centripetal force, which in collaboration with surface tension, evenly distributes the ink

in a thin liquid layer and causes the majority of the liquid precursor to fly off the substrate as seen in Figure 11. The remaining solvent then fully evaporates, leaving a thin uniform film composed solely of the desired solid composition [53]. The thickness of the film is a function of the ink viscosity, drying rate, solid concentration, surface tension and spinning parameters such as speed and time interval [54]. This has been used to form perovskite active layers in cells with efficiencies of about 22.1% but ending up at the question of scalability. Spin-coating is traditionally, a non-scalable process. The spin coating method is inherently a single batch process and therefore not scalable to large volume production and involves substantial waste. Each substrate would have to be produced individually. Due to the very high velocities, torques and the potential for catastrophic failure that can exist for spinning large area substrates at high rpms, spin coating is also fundamentally limited in process area per step.

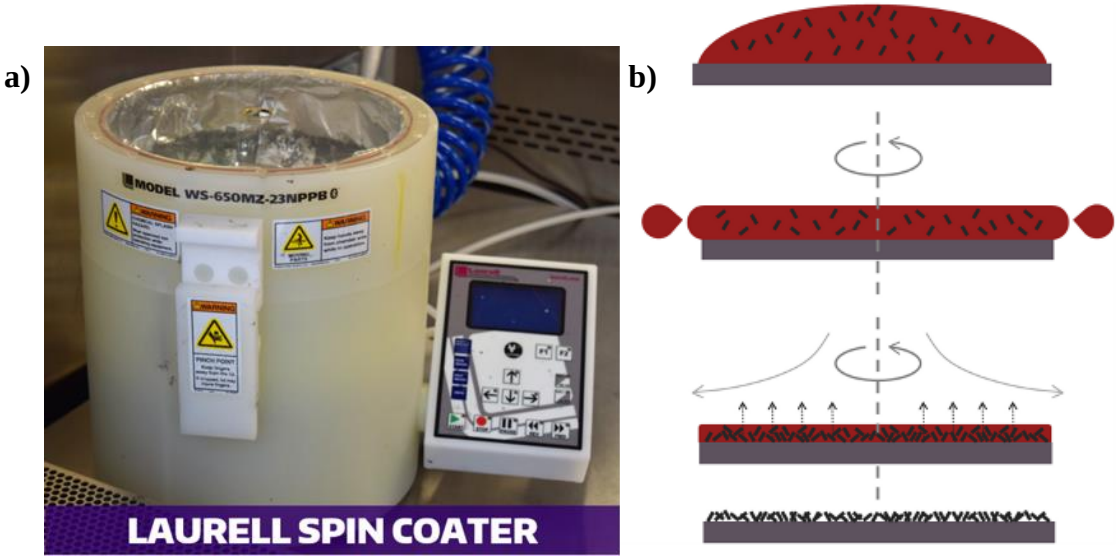

Figure 11 a) Lab scale spin-coater, b) Spin coating process from beginning to end

Furthermore, current lab scale spin coated perovskites are typically limited to an active area of 1 mm^2 to 4 cm^2. As perovskites begin to move towards mass production, individual cell size and production volume capabilities must increase substantially. While it is possible to spin coat substrates ranging from a mm^2 to 0.1 m^2 scale, the process tends to result in film quality issues with increasing area and involves large materials waste and yield risks associated with catastrophic failure at very high torques.

Spin coating also does not provide the option to directly pattern layers. It would require additional subtractive patterning steps such as lithography in order to pattern the active layer. The high volume of material wasted and the lack of scalability with the spin coating process is problematic and opens up opportunities for exploration of other active layer production methods that are scalable to a roll to roll setup.

4.3 R & D Flat sheet coater

In this research, the FOM R & D sheet coater is used, where a slot die coating method is adopted to fabricate perovskite solar cells. This process is chosen because of the ability to be directly translated to a scalable manufacturing method like the roll-to-roll process, its low materials wastage, and an environmentally-protected ink supply system. The FOM flat sheet coater offers numerous parameters to optimize the printing process based on the need of the user making this a multivariable research project.

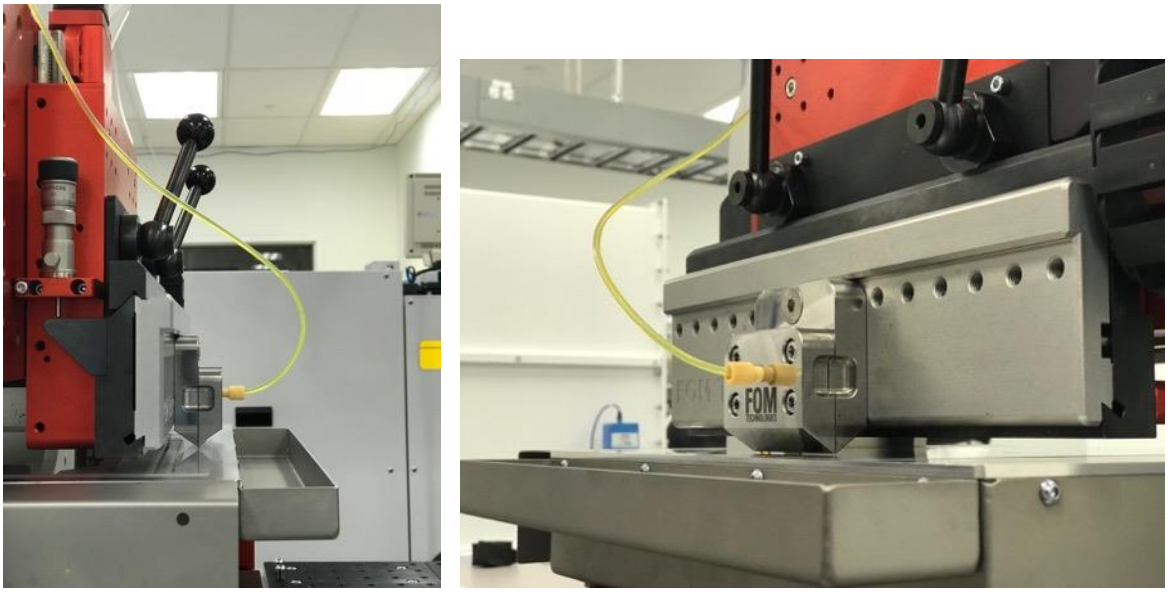

Figure 12 The FOM technologies R & D sheet-coater at the Washington Clean Energy Testbeds

The slot-die head consists of a shim that is sandwiched between two stainless-steel blocks. The target ink is fed to a slot die through a tube by using the syringe pump that stores the perovskite ink which is placed on the top of the coater. The pump and withdrawal

rates play a vital role in the first step of the coating process, in forming a meniscus with the substrate. The syringe pump has four controls namely:

- F1- Fast withdrawal
- F2- Slow withdrawal
- F3- Slow infusion
- F4- Fast infusion

The substrate is positioned on the vacuum assisted bed of the sheet coater after which a meniscus is formed by using a combination of the above controls and lowering the slot-die head to create a liquid to substrate contact through capillary action with ~38 µm separation (arrived at after experimentation). The programmable bed is moved horizontally, and the coating action is completed with very little loss of ink by meniscus-assisted extraction as the bed moves under the slot-die head with the set coating speed. Due to the coffee ring effect, the solutes are pushed towards the meniscus-air-substrate contact by forming grains as the bed moves, which is partially due to an outward convective flow (away from the meniscus) created to compensate for the instantaneous solvent evaporation from the meniscus [55]. The ink dispensing parameters are controlled by the syringe pump using feed/withdrawing controls. After the film is coated, the ink is withdrawn, and the meniscus is cleared after which the slot-die head is raised.

The position of the slot-die in the x, y-direction is controlled using a spindle. The coating process depends on a variety of factors such as the bed temperature, bed speed and the ink-dispensing rate. In addition to this, factors related to the substrate quality, ink system and meniscus profile hugely affect the resulting film. The pump rate and the speed are iterated to get a desired wet film thickness.

$$\text{WFT } (\mu\text{m}) = \left[\text{pump rate } (\mu\text{L/min}) \Big/ \text{bed speed } \left(\frac{\text{cm}}{\text{min}}\right) \right] * \text{die shim width (mm)} \qquad (3)$$

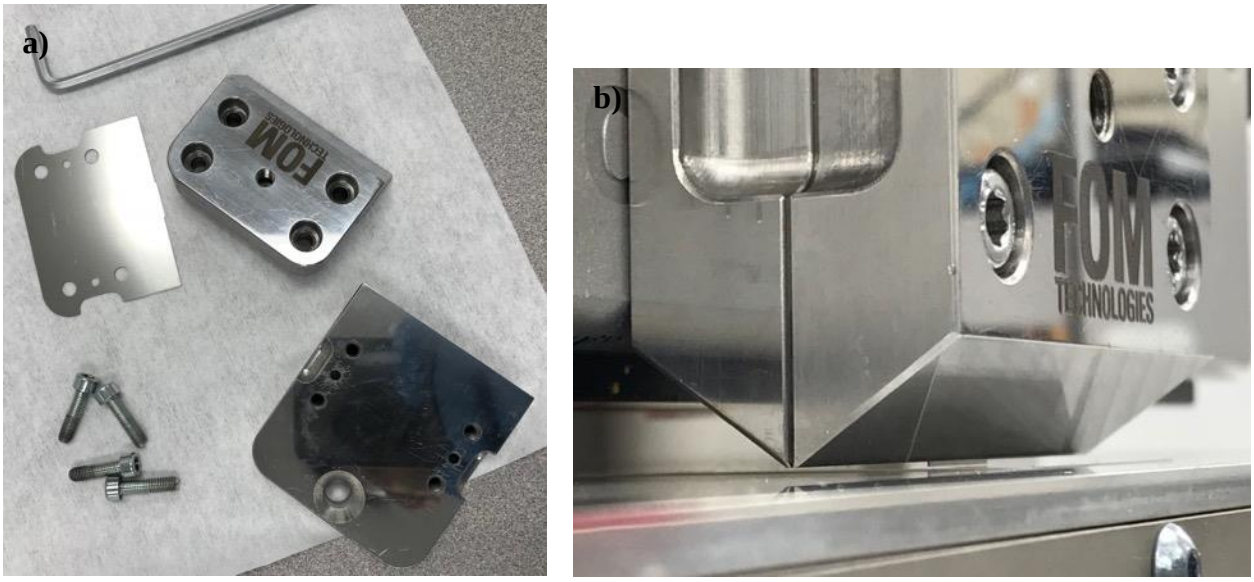

Figure 13 a) The slot-die head, with its three parts: shim and 2 coating heads b) An up-close image of the slot-die head maintained at a 50 um height from the flat-bed

All coating related functions such as substrate bed temperature, speed, pump rate, coating process (execution, diptray movement, start point, coating length and pump control) are changed using this software. All coating recipes containing this information are stored, ready to be loaded, edited or used in accordance with the user.

Figure 14 Syringe pump used to dispense perovskite ink

4.4 Perovskite printing

A second step in the conversion of PbI_2 to perovskite films in the two-step deposition method can be eliminated by using the slot-die deposition method as reported by Giovanni et al. [31]. Cells fabricated using this method resulted in a maximum PCE of 11.96% with a device stack of ITO/ZnO/perovskite/P3HT/Ag when coated at a bed temperature of 70ºC [56], which has a beneficial effect on the charge separation layers when printed using the slot-die process. Due to the relatively slow process with multiple independently controllable variables, functional layer slot die coating can be optimized easily, and one can gain better control over the deposition process than spin-coating methods. Successful fabrication of high efficiency solar cells using the slot-die implies a direct translation of the process to the roll-to-roll printer. A dry thickness value for the printed film can be estimated by using the relationship between the fluid flow rate (f cm^3/min) and the bed speed (B_s cm/min) with the coating geometry (width as w cm), solute concentration (c g/cm^3) and density of the ink material (ρ g/cm^3) [57]

(4) $$d = \frac{fc}{B_s w \rho}$$

5. Environmental chamber with constrained N_2 flow

I will be looking at the introduction of a processing step in open air slot-die coating that utilizes nitrogen flow in a self-designed enclosed chamber as seen in Fig. 8, to regulate the film morphology and microstructures. A recirculation zone developed in the chamber assists in fast solvent evaporation and accelerates the drying of the printed layer. Introduction of nitrogen helps minimize oxygen content and moisture interaction with the film aiding in a layer free of possible defects induced by the same. In a constrained N_2 flow setup, nitrogen is passed through an enclosed chamber just above the substrate, via a 3/8” pipe from the gas blow-off from a compressed liquid nitrogen tank. Nitrogen then enters the chamber via an Exair 1” flat air-nozzle in the prototype chamber talked about in section 5 and a 12” Exair Standard Air-knife with a 0.002” opening in the final design. The chamber encloses the slot die head, which dispenses ink on to the substrate. Introduction

of N_2 creates a recirculation zone within the chamber, forcing the moisture laden ambient air out of the control area. This keeps the wet perovskite layer from interacting with moisture and oxygen, allowing it to successfully convert to a desired perovskite layer in the absence of ambient air. The N_2 inlet pressure and bed temperature are important factors that control this conversion process. The coated layer is not entirely dry, and the formation of crystals have not initiated.

Following are the experiments conducted to appropriately establish parameters for printing in the presence of N_2 flow and design the final chamber based on issues developed using the prototype chamber.

- To determine an appropriate inlet pressure for nitrogen.

  I. A 25 wt % solution of MAI+PbI_2 was coated on a PET substrate, with the slot-die enclosed by the chamber and the inlet pressure varied from 3 psig to 25 psig. In two different experiments, films were coated at the same web speed with a 5ºC difference in the coating temperatures. The film coated at 90ºC with 3 psig inlet pressure was 13nm thicker than the film coated at 95ºC with 5 psig inlet pressure. As the dependence of the coating temperature on film thickness is a weak factor than N_2 velocity in the chamber, the difference in the film thickness can be attributed to the variance in inlet pressure for N_2 flow.

  II. The films coated at 3 psig inlet pressure showed light and dark regions that extended across the film. Further experiments show that when the inlet pressure was ramped up, the dark region shifted to the left portion (normal to the coating direction) of the film (5 psig) till it disappeared (25 psig). The scattering of drops that can be seen on the film can be avoided by iterating the N_2 inlet pressure (17-23) psig and the bed coating speed with added design alterations in the chamber.

With the prototype chamber, an inlet pressure greater than 10 psig always resulted in scattering of the perovskite ink rendering the coated films unusable. Pressures below 10psig and above 5psig ensured good quality perovskite films with no pinholes. The light

and dark regions in the films disappeared when the new chamber design was used. More about experiments incorporating this design will be talked about later in the document.

Controlled N_2 flow in the deposition chamber hopes to achieve:

- Quick drying by means of evaporation of the solvent. The faster drying rate will be induced by flowing nitrogen.
- The recirculation zone that forms in the chamber promotes consistent solvent evaporation which helps in perovskite crystallization by uniform conversion to an active perovskite layer. The conversion here refers to wetting of the surface and subsequent grain formation around nucleation sites.
- Minimal interaction with O_2 and moisture due to continuous flow of N_2 maintains optimal humidity conditions in the control volume, perfect for perovskite coating in ambient-air.
- To gain control over grain size, film quality and evaporation rate to assist in slot-die printing of perovskites

5.1 Chamber

Two chambers were designed. Initially, a small-scale prototype chamber was fabricated, and experiments are conducted with variations of the perovskite precursor solutions and the NiO_x hole transporting layer. Based on constraints set by this chamber, a large-area final chamber was fabricated for the following reasons:

- **To analyze the effect of change in the distance of the N_2 flow source from the coating head.**
- **To use a 12” long standard air-knife which ensures flow over the entire bed on which the perovskite film will be coated.**
- **To prevent scatter when the N_2 inlet pressure is raised above 10 psig.**
- **An adjustable air-knife angle, allowing different angles of N_2 flow impingement on the substrate to be studied.**

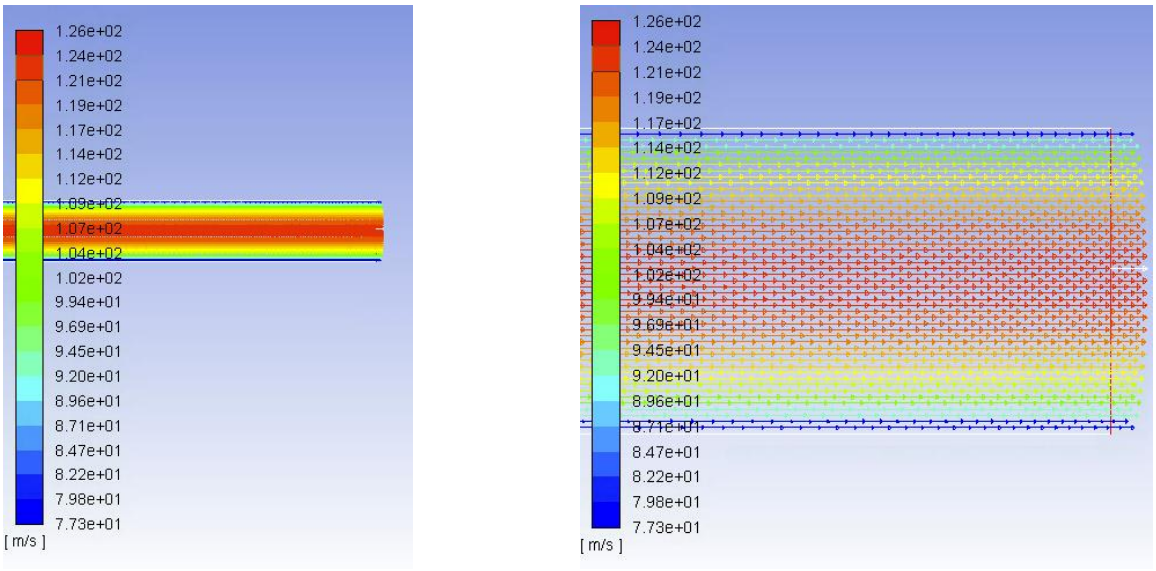

Figure 15 Simulation of the 3/8" pipe inlet to the air-knife

The outlet velocity from the 3/8" pipe equals 126 m/s, as simulated on ANSYS 18.1 seen in Figure 15. As the Exair air-knife has a flow amplification ratio of 30:1 [58] due to entrainment of stationary gas from the surroundings, this reduces the velocity of N_2 to about 20.3 m/s at the bed surface at 15 psig inlet pressure. This value agrees with the specifications published in the air-knife catalogue [25.4 m/s @20 psig inlet pressure, 6" away from the air-knife].

5.1.1 Prototype chamber

The N_2 flow directed from the air nozzle aperture is primarily deflected parallel to the surface of the bed which is directed to the upper most zone and interacts with air streams

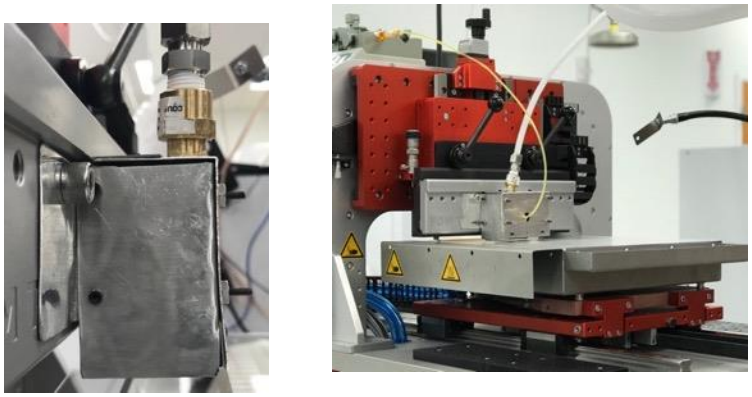

Figure 16 Picture of the prototype chamber in operation

already present in the chamber as seen in Figure 17. This continued time-dependent interaction of N_2 and air in the chamber is the reason for the recirculation zone development. The N_2 that flows vertically and hits the bed, drops to zero velocity creating a low-pressure zone (stagnation point). The extreme left of the chamber houses the VWR air-nozzle and a circular inlet in the center allows a tube from the syringe that stores the ink to connect to the slot die head through which ink is dispensed onto the substrate.

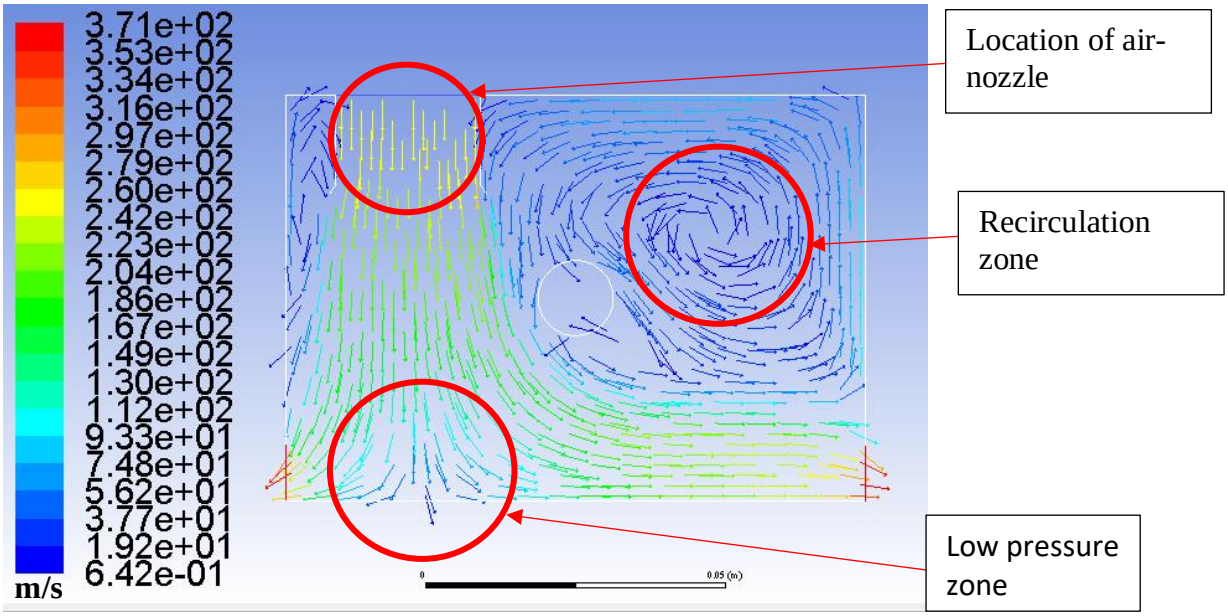

Figure 17 Simulation of air-flow within the prototype chamber

An initial prototype of the environmental recirculation chamber is fabricated using 0.84 mm thick aluminum sheets. N_2 is hypothesized to act as a drying agent, that accelerates the evaporation of the DMF solvent and hence the box design was centered on the idea that compressed N_2 entering the box plays a role in increasing the rate of evaporation of the Dimethylformamide (DMF) solvent in Perovskite films. The constant airflow also smoothens out the coated layer [35], flattening out any undesirable contours formed on the substrate, which is validated by smoother films. The absence of pinholes in the layer, coated in the presence of N_2 can also be attributed to this phenomenon. The flattening out improves the coat quality of the perovskite film, evidenced by uniform, homogeneous layers with better surface coverage.

5.1.2 Final chamber

The N_2 collides with the bed and gets deflected upwards creating a recirculation zone in the center of the chamber. The perovskite solution interacts with the N_2 after conversion by entering the recirculation zone and stays there during the annealing procedure. The air-knife is placed about 11” away from the coating head, with the mouth of the nozzle pointed 5” away from the bed surface when in the tilted orientation.

Figure 18 Picture of large area chamber in operation and with an air-knife a)Distance from the coating head to the air-knife b)Distance from the top of the air-knife to the bed

5.2 Process of fabrication

A rectangular chamber enclosing the entire bed is designed using 0.08” thick 6061 aluminum sheets. The sheets are joined using corner brackets and 90° braces which were cut using the OMAX abrasive water jet cutting machine at the Wilson Ceramic Laboratory of the Material Science and Engineering Department. An initial design was created in SketchUp Pro 2018 and the component drawings were made in SolidWorks 2017

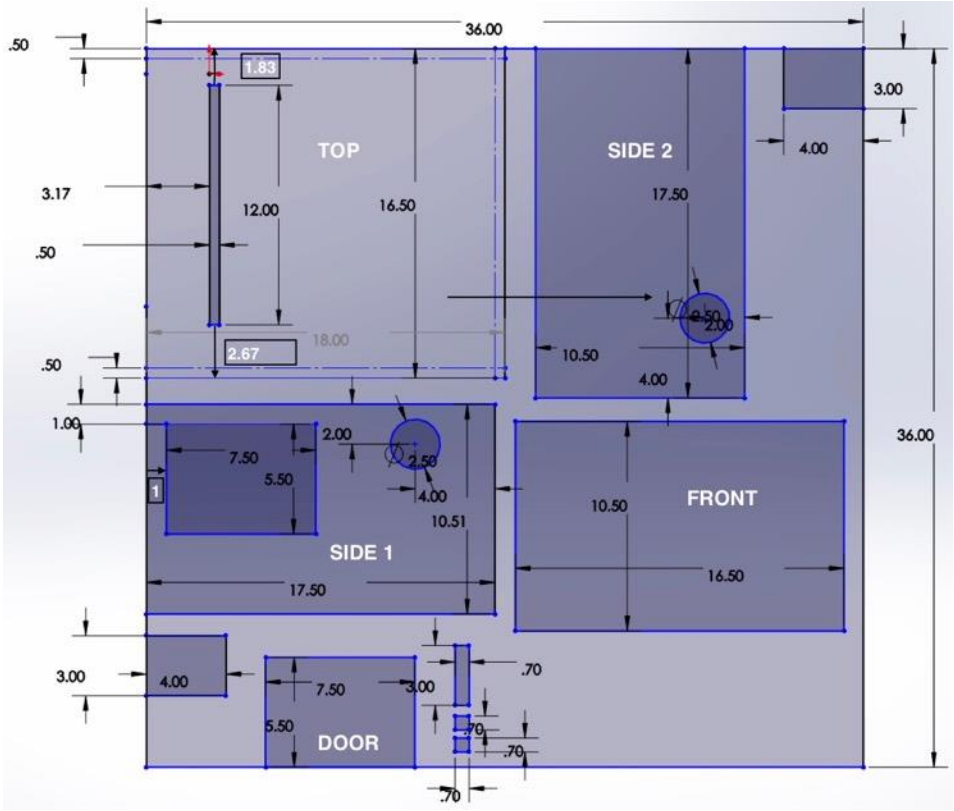

Figure 19 Drawing with measurements in inches for the final chamber components

The air knife is mounted on a hollow circular tube of 1” OD with a 0.25” wall thickness and receives N_2 through a pipe. The tube can be rotated at different angles such that the mouth of the air-knife faces the bed of slot-die coater to achieve a shift in the natural recirculation pattern. In this setup, the perovskite layer that undergoes conversion interacts with the N_2 flow allowing the DMF solvent to evaporate with ease gradually increasing the evaporation rate as the recirculation zone fully develops.

6 Experimental section

6.1 General experimental setup

The substrate is positioned on the bed of the flat sheet coater, which is then cleaned by a Teknek fast-pad to remove stray dust particles and lint. Typically, a 6ml syringe is used to store the perovskite ink. A tube of diameter 3.15 mm is fed to the slot die from this syringe. An exhaust is switched on to lead the toxic DMF vapors to the atmosphere. This completes our experimental setup and the coating process can now be initiated.

Coating experiments indicated that the meniscus formation was the most crucial step that affected the coating pattern. A wide meniscus exceeding 13 mm leads to widening of the coating strip leading to an unevenly distributed coat. A narrow meniscus leads to a contact break during the coating process, resulting in an unfinished coat. For printing in the presence of N_2, the environmental chamber is placed over the bed, the N_2 lines are connected and coating is resumed.

6.2 List of solutions used

The perovskite precursor ink that is used majorly throughout the research project was a solution made by dissolving MAI crystals from Great Cell solar and PbI_2 (99.9985% metals basis) from Alfa Aesar in a DMF solvent at a 1:1 molar ratio. The solution was left on a stirring station overnight while being stirred with a magnetic stir bar at 1000 rpm. The resulting solution is a yellow colored and optically clear perovskite precursor solution.

Concentration	Solvent	Markers
10 wt %	1:10 NMP:DMF	
15 wt %	DMF	0.3 M of CH_3NH_3Cl
10 wt %	DMF	0.3M excess of CH_3NH_3Cl
25 wt %	DMF	1:1 MAI and PbI_2

Table 2 Perovskite solutions used to arrive at the desired precursor solution

6.3 Cleaning method

The PET substrate was cleaned by a 2% DI+ a non-corrosive, non-abrasive detergent (Micro 90) solution after which it was rinsed by distilled water and dried using an N_2 air-gun. The substrate was then cleaned with isopropyl alcohol followed by drying using the N_2 air-gun which is then treated in a UV-ozone cleaner for 10 min with an exhaust time of 10 min to remove contaminants like dust, cleaning residuals, oils and organic residues. UV-ozone treatment also helps in increasing surface wettability and eliminates problems associated with dewetting.

6.4 Experiments and Analysis

Several perovskite solutions are coated with varying parameters to arrive at a solution composition that works best with the slot-die coating method both with and without N_2 flow. These solutions were prepared based on literature review and work done by researchers at the Washington Clean Energy Testbeds. These films are characterized based on microscopy and spectroscopy methods. In addition to coating perovskite solutions, coatings from different compositions of the Hole Transport Layers (HTL) are also executed and studied in this section. Different variations of perovskite solutions and ETLs are prepared and printing is done by adjusting the print parameters based on observation and spectral analysis of the perovskite print layer quality.

Perovskite coating on poly(3,4-ethylenedioxythiophene) polystyrene sulfonate (PEDOT:PSS)

PEDOT:PSS is a ductile conductive polymer that finds uses in different applications. It has been effectively used as an HTL in perovskite solar cells. PEDOT:PSS was coated using the R & D flat sheet coater on a PET substrate. In order to prepare solar cells based on a planar heterojunction architecture using the slot-die method, coating perovskite on top of the HTL was suggested, as the nature and quality of PEDOT:PSS film surface can play a major role in dictating the quality of perovskite layers printed [59]. As

observed in the experiments, it was concluded that UV-ozone treatment is necessary with a 10 min cleaning time, accompanied by a 10 min exhaust time to avoid dewetting.

Initial NiO_x nanoparticles coating on old PET

NiO_x nanoparticles play an important role as an inorganic bottom and top-hole extraction layer in PSCs [60] and low temperature printing method for the same needs to be explored. One of my lab colleagues synthesized NiO_x nanoparticles by dispersing 3 g of $Ni(NO_3)_2 \cdot 6H_2O$ in 60 ml DI water after which its pH was adjusted to 10 by adding 0.5 mol L^{-1} (Sodium Hydroxide) NaOH solution. A green colloidal precipitate was formed which was thoroughly washed twice with DI water and ethanol and dried overnight at 80°C. The green powder was ground and calcined for 2 hrs at 270°C. The resulting black powder was then dispersed again in DI water with a concentration of 20 mg/mL.

The measured surface roughness for the coated films is **86.2 nm** which is over the limit of what is desired. A surface roughness value close to $1/10^{th}$ of this value is required for our application. This can be brought about by iterating print parameters and experimenting with drying mechanisms. A change to a smoother 125 µm MELINEX ST505 heat stabilized PET was made on which all further coatings were done.

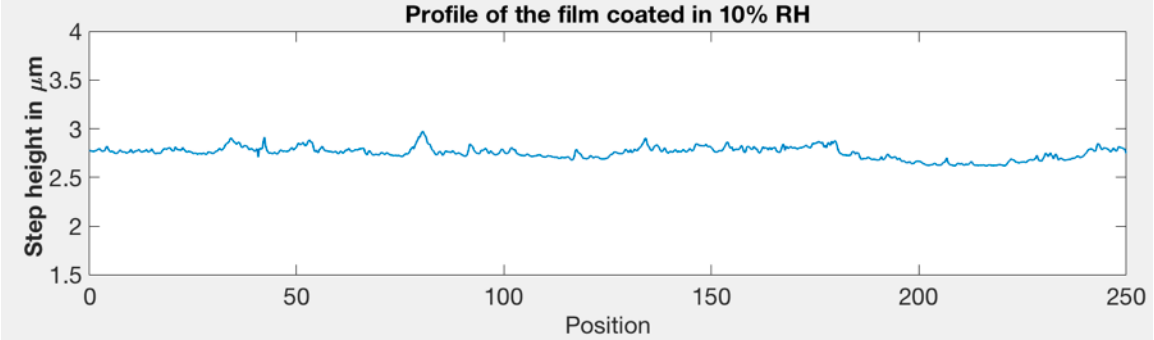

Figure 20 The above plot shows the surface profile of the NiO_x coated film.

Coating a variation of the Perovskite solution on Nickel oxide nanoparticles

Objective: To observe perovskite films coated over the HTL

A 10 wt % perovskite precursor solution in a 1:10 NMP:DMF solvent is coated on slot-die coated nickel oxide nanoparticle HTL layers on a PET substrate. This is done to provide a platform to optimize the print parameters for perovskite coating on top of the HTL and also characterize the nickel oxide nanoparticle layer visually and arrive at its printing parameters. The substrate bed temperature was varied from 80°C to 110°C and the bed speed was kept constant at 150 cm/min. The perovskite layer coated at 80°C converted instantly from **right to left** with the film resulting in a dark brown color. When the film was coated at 85°C, it developed in much lighter shade than previous perovskite coatings.

Figure 21 Perovskite layers printed over the NiO_x HTL

NiO_x nanoparticle layer optimization

Objective: To investigate the effects of coating temperature on NiO_x printing

To improve the morphology of the perovskite layer coated, the film below the perovskite layer must be free from voids, pinholes and any particle aggregations that could cause excessive valleys and peaks in the active layer thickness. NiO_x nanoparticles in isopropyl alcohol (IPA) were coated on a MELINEX ST505 heat stabilized PET. Coatings were done by raising the temperature from 65°C to 100°C and lowering the bed speed from 200 cm/min to 150 cm/min in a series of 9 print layers. The films coated at 75°C and 100°C at 150 cm/min bed speed were smoother and did not show any aggregates on the surface.

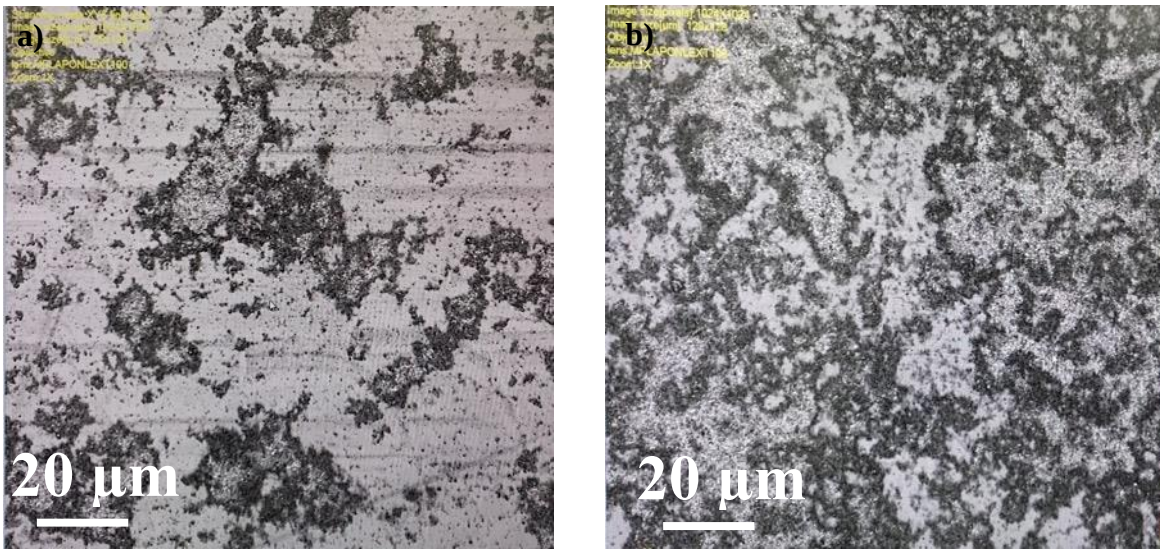

Figure 22 a) Coat #4; b) Coat #9 (75°C and 100°C, 150 cm/min)

In a following experiment, nickel oxide nanoparticles were coated on glass at 100°C with varying speeds. The film coated at a coating speed of 200 cm/min visually appeared uniform and homogeneous with an average root mean square surface roughness of **49 nm**. This value is much higher than the desirable value to ensure a perfect active layer coat.

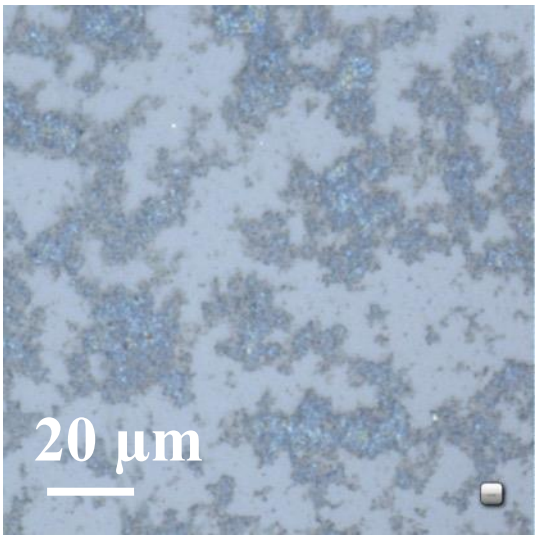

Figure 23 Laser microscope image of Coat #5 with 49 nm (100°C, 200 cm/min)

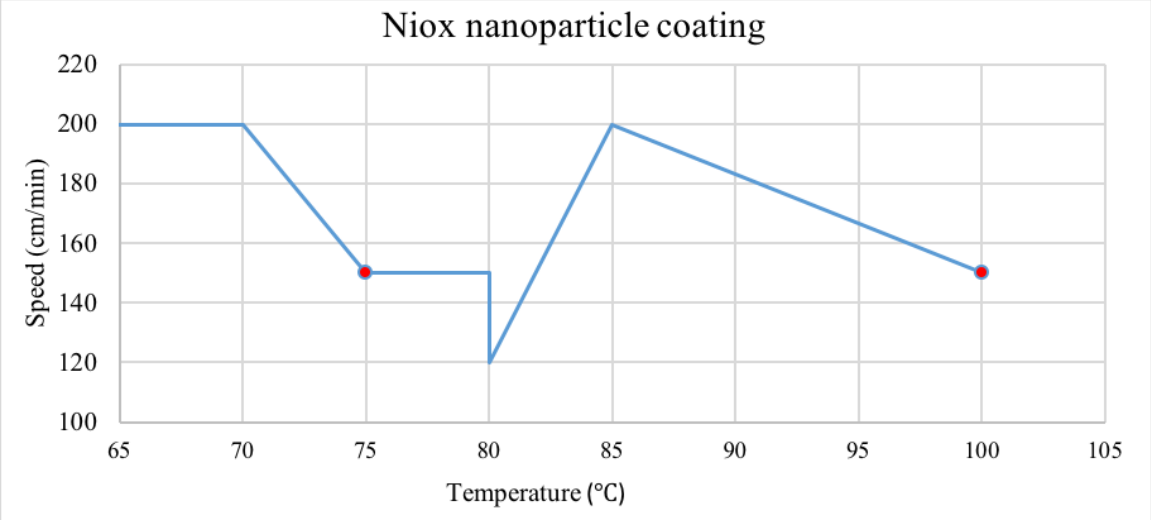

Figure 24 Iterating printing parameters for NiO_x films

It is seen that the film coated at a speed of 150 cm/min was homogeneously distributed and free from particle aggregation. The high temperature and high speed coating of the nanoparticle solution was also done in the presence of constrained N_2 flow. The resulting film had a lower surface roughness of about 53 nm compared to films coated in the absence of N_2 (72 nm and 64nm). They also had uniform particle distribution and minimal aggregate formation as seen in Figure 25.

When the nanoparticle solution was coated at substrate bed temperatures above 100°C, it resulted in films with surface roughness values of 48 nm, 72 nm, 64 nm. In the last case when the film was coated at 150°C in the presence of N_2 flow, the surface roughness measured was **53 nm**.

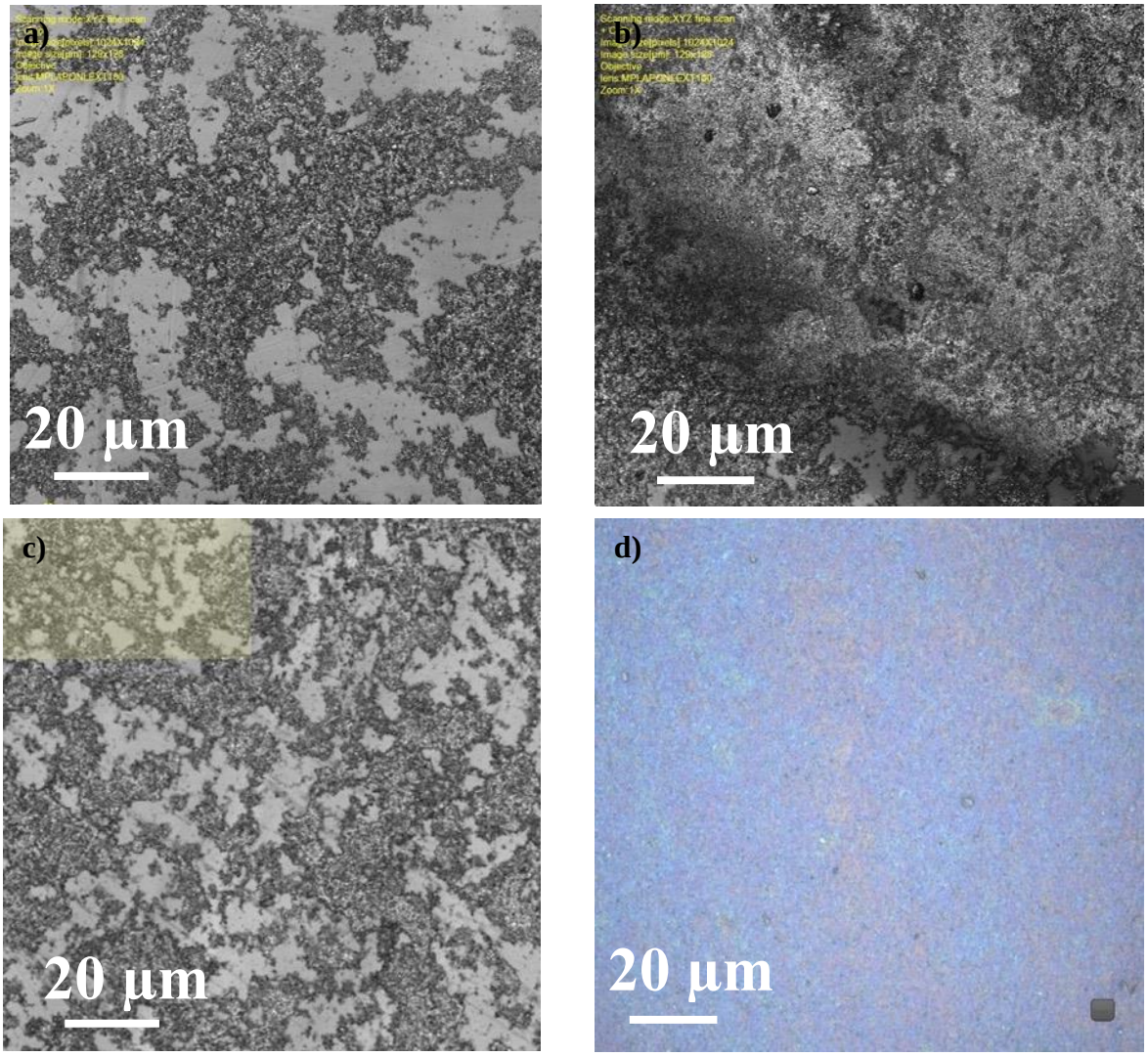

Figure 25 a) 120°C, b) 140°C, c) 150°C, d) 150°C with N_2) [Yellow shaded area represents the area chosen for surface roughness measurement]

Although high speeds and high temperatures give good results, it is difficult to control the coating process in terms of maintaining a stable meniscus for printing. Also, high temperatures can lead to nanoparticle damage. Hence, further experimentation is done to bring down the temperature and coating speed.

In an attempt to increase the drying rate of the film, diluting the solution in isopropyl alcohol is suggested. A 2.5 ml solution of 1:5 NiO_x+H_2O+IPA and 4.5 ml of IPA were mixed to get a 1:6 NiO_x: IPA cloudy grayish colored solution.

Coating with 1:6 NiO_x: IPA solution

This solution was coated on a PET substrate with the temperature varying from 65°C to 120°C with the bed speed constant at 200 cm/min. For this solution, the film with best coverage of nanoparticles was the one that was coated at 115°C and 120°C. The poor coat quality for the other films were partially because of the high particle sizes of the nanoparticles. The particle sizes as measured by researchers using Dynamic Light Scattering (DLS) on the Anton Parr Litesizer™ 500 particle analyzer averaged to about 400 nm which posed undesirable. Particle sizes of 3-10 nm is best suited for our application.

Nanoparticles coating in the presence of N_2 flow.

Objective: To investigate N_2 flow printing for NiO_x films

Perovskite precursors were initially coated in the presence of N_2 and interesting results were observed in the film; To investigate this premise further, NiO_x nanoparticles were also coated in the presence of N_2. NiO_x nanoparticles suspended in H_2O were coated on a glass substrate by the FOM flat sheet coater using the parameters below.

NiO_x **printing parameters:**

Coat #	Temperature	Speed (cm\min)	N_2 flow
1	65	120	No
3	67	120	No
9	65	120	Yes

Table 3 NiO_x printing parameters

The coat #9 appeared to be homogeneous, uniform and less rough compared to all other coats which can be attributed to faster drying time of the coated nanoparticle layer owing to flow of N_2 over the layer during the coating process. As evidenced by the images taken on the SEM and LEXT, N_2 takes away the solvent molecules from the coated film, leaving it with only a transparent layer of NiO_x nanoparticles. The nitrogen also helped in

smoothening out a thick nanoparticle layer leading to a much smoother and less rough layer with a surface roughness of **5 nm**.

To validate the significance of drying to ensure a homogeneous and smooth coat, NiO_x nanoparticles with IPA was added in 3:2 ratio and was coated in the humidity control room without N_2 flow at a relative humidity of **10%**, keeping the print parameters constant. This resulted in a coat with a surface roughness of **4 nm**.

A low value of relative humidity played a significant role in maintaining the drying mechanism even in the absence of constrained N_2 flow. **This experiment comes to a premise that constrained N_2 flow during coating NiO_x particles plays a similar role and provides similar conditions as 10% relative humidity based on results from film characterization**. Freshly synthesized nanoparticles and coating within 24 hrs of synthesis ensured that the coated layer was free of areas of particle aggregation. In addition to this, maximum particle size distribution fell mostly in the range of 12-15 nm as measured by DLS

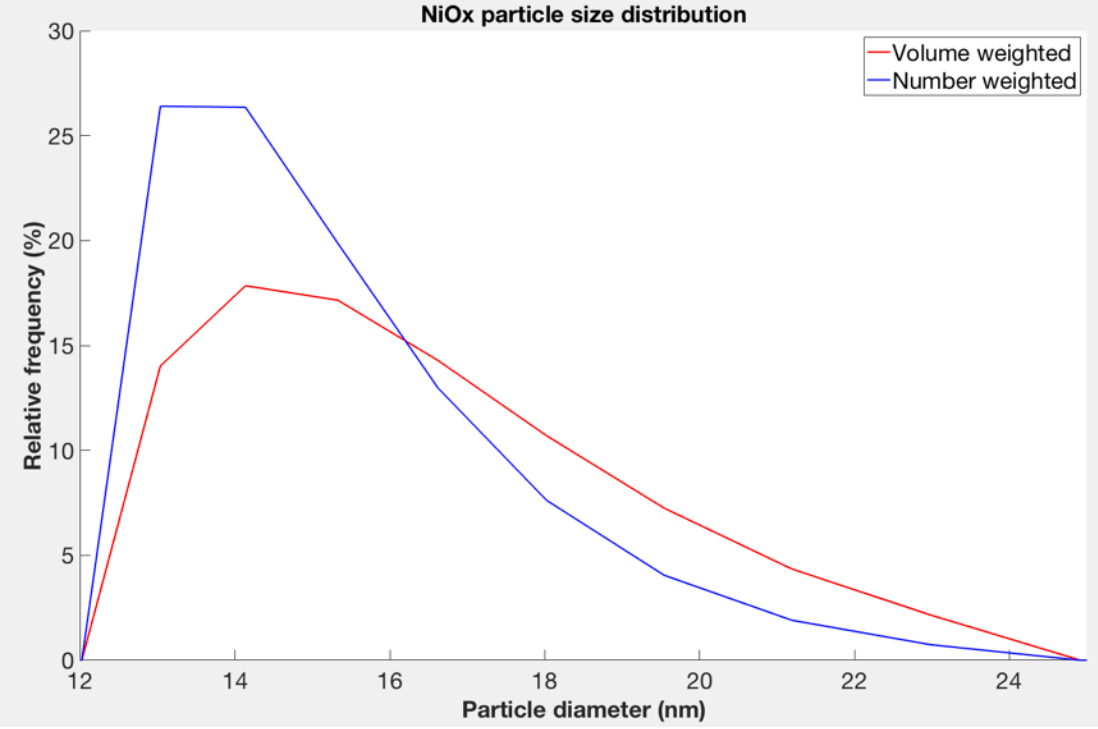

Figure 26 Particle distribution of NiO_x nanoparticles as measured on the DLS

Perovskite coating at varying temperatures with and without N_2 flow

Objective: To verify if N_2 is a good candidate to decrease drying time and conversion time from the perovskite precursor solution to a photoactive perovskite layer.

The initial perovskite precursor solution used included an excess 0.3 M of 54g of Methyl ammonium chloride (CH_3NH_3Cl) in 4.3 ml of 15 wt % Methyl ammonium lead iodide solution [46]. This experiment is conducted at a bed temperature of 23.3ºC, bed speed of 100 cm/min without N_2 flow, the coated film failed to convert and resulted in a dark grayish film which took about 3s to dry. Whereas in the case when N_2 flow was present during coating with the bed temperature raised at 23.3ºC with rest of the parameters kept constant, the film converted instantly. The coating process was followed by an air-annealing step on a hot plate for 150ºC and the second film which was coated in the presence of N_2 flow converted to a desirable film with a brown color saturated with reddish areas. It is seen that nitrogen is promising in improving the quality of the perovskite layer.

Issues: The coated films took too long to convert, around 30s. The coating temperature needs to be iterated to result in a desirable grain formation

Perovskite solution with different concentrations

Objective: To study the effect of temperature on Perovskite coating

A lower concentration of 10 wt % perovskite solution in DMF with 0.3M excess of CH_3NH_3Cl was coated on PET substrates with the bed temperature in the range of 23.3°C to 80°C. After the first layer was coated, the bed speed was increased to 150 cm/min from 70 cm/min. The first layer converted to a dark grayish color after annealing at 150°C on a hotplate. When the bed temperature was raised to 82.6°C with the coating speed at 150 cm/min after 100°C thermal annealing, the film converted to the desired reddish-brown color with large grain sizes as observed on the SEM. When the last film was coated with the above parameters fixed but photonically annealed using a flash lamp, the grains reduced in size and appeared to be closely packed. The thickness of the non-annealed perovskite layer was measured Olympus OLS 4100 3D confocal laser microscope.

Annealing method	Surface roughness (nm)
Non-annealed	318
Thermally annealed	272
Photonically annealed	400

Table 4 Surface roughness of films annealed by different methods

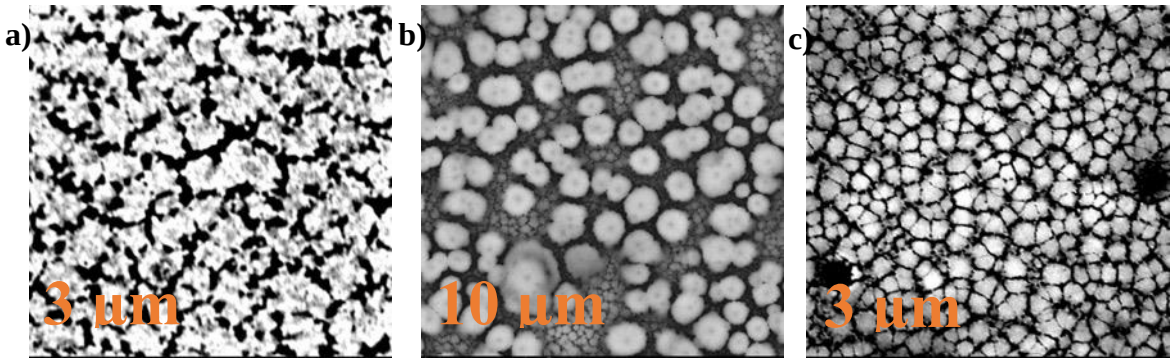

Figure 27 a) Thermally annealed; b) Photonically annealed; c) Photonically annealed

Image analysis: The grains have not developed fully and there exists wide grain boundaries and numerous zones of no-grain formation, but a higher temperature than ambient is observed to produce close to desirable coats. It can be seen from the measurements that photonic annealing induced vertical growth in crystals.

Perovskite coating in the environmental control room

Objective:

- To analyze the influence of humidity on perovskite coating [34].
- Arrive at a coating temperature for perovskites

The environmental control room at the WCET is equipped with controls to regulate the humidity and temperature in a 45 m^2 lab area. The perovskite precursor solution in 1:10 NMP:DMF 10 wt % by weight is coated on the 125 µm MELINEX ST505 heat stabilized PET in the control room with varying relative humidity levels

Coating is done at 100°C and 95°C with the coating speed set to 150 cm/min and a relative humidity of 10-60 %. The film coated at 100°C in 10 % and 15 % humidity converted instantly and resulted in a uniform coat free of pinholes. The annealing process followed was a thermal annealing step at 10 % RH at 100°C for 5 min on a hotplate. The film coated in 15 % RH was the best in terms of coat quality. Further analysis was not possible on the films as they began to degrade gradually after the coating ended.

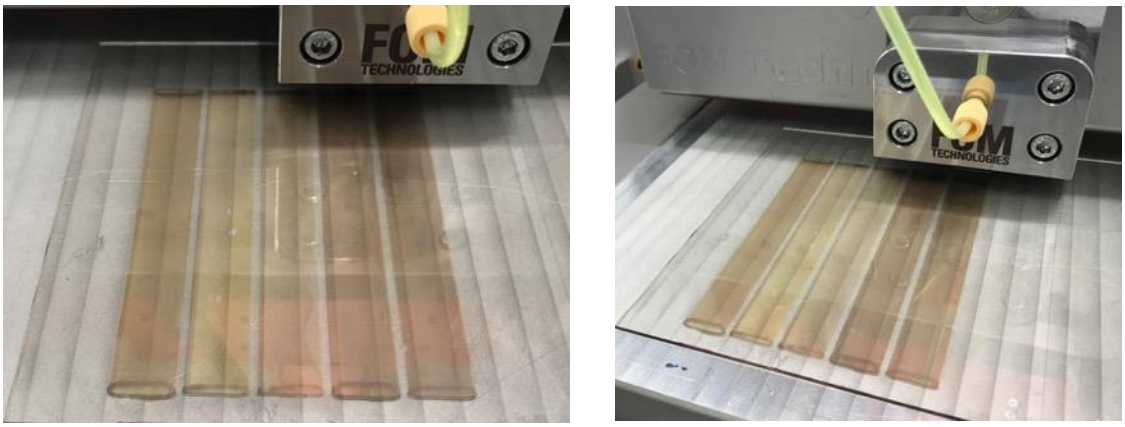

Figure 28 Coated perovskite layers from left to right (10% RH, 15% RH, 30% RH, 45% RH, 60% RH) respectively

Image analysis: The coated layer in Figure 28 looks acceptable in terms of coat quality. The coated layer is free from pinholes and dewetting zones.

Issues: The coats began to degrade gradually preventing any further optical analysis

New perovskite precursor solution

Based on the weight concentrations used in literature, a 25 wt % solution made with 1:1 MAI and PbI_2 dissolved in DMF was prepared and is decided to be used in further experiments.

Variation of temperature with constant N_2 flow pressure of 3 psig to calculate the gas thickness

Objective: To calculate the gas thickness value for complete evaporation of DMF and to evaluate an optimal temperature for perovskite grain formation

The coating speed was kept constant at 150 cm/min and the temperature was raised from ambient (25°C) to 95°C. Coating was done at temperatures ranging from 25°C to 95°C with an increment of ΔT of 5°C with every coat.

The experiment was resumed with substrate bed temperatures ramped to 45°C. At this temperature, the coat took about 3-5s to fully convert to a $MAPbI_3$ film. It was at 70°C, that the coated precursor solution took less than 1s to fully convert. The converted film had a mirror like appearance with a thick black coat. Reddish brown films started appearing when the coating was done at 80°C, with a perfect dark brown color coat with a reddish tinge at 85°C with less than 1s conversion time.

The film at 85°C was viewed through the LEXT Olympus OLS 4100 laser microscope and a film thickness of 952 nm on the right half of the film and 762 nm on the left half of the film was measured. At 90°C, the films retained a similar morphology, but the surface roughness decreased to 56 nm on the right half of the film and 179 nm on the left half of the film. This also helped in deciding the coating temperature for perovskites which was decided to be in the range of 90°C and 95°C, as at these temperatures the films displayed a uniform and homogeneous morphology with low surface roughness. This temperature also favored faster conversion times which is detrimental to perovskite crystal formation.

Calculation for gas thickness

Gas thickness: This is a necessary condition for evaporation of the solvent in the precursor solution. The solvent completely evaporates till its partial pressure reaches the saturated vapor pressure at the current temperature in the control volume. The value at which this occurs, completely removing the solvent vapor from the solution is referred to

as critical gas thickness. Hence our value of the critical thickness must be greater or equal to this for complete solvent evaporation [35]. The gas thickness value for the DMF solvent in a volume of 2 ml was calculated to be 0.268 nm at 95ºC (368 K) using the equation below. A volume of 2 ml was chosen based on the volume stored in the syringe pump to be dispensed onto the substrate. The fast conversion time of the precursor solution to an active perovskite layer is postulated on the theory that the solvent leaves the substrate after coating, almost instantaneously and thus the value of *P* (Partial pressure of the solvent) can be calculated.

(5)

$$P = \frac{nRT}{V}$$

where *n* is the number of moles of DMF, *R* is the gas constant in L atm mol-1K-1, *T* is the temperature of the flat bad in K and *V* is the volume of the solvent in L.

(6)

$$H = \frac{\rho_1 w\% RT}{P * M} \partial$$

where ρ_1 is the density of the precursor solution, w% is the concentration of the perovskite precursor solution, M is the molar mass of the solvent, and ∂ is the wet film thickness. As we had observed the best quality perovskite films at 95ºC (368 K), the gas thickness value was established at this temperature. It is predicted that the DMF vapor completely evaporates from the film at a gas thickness of **0.268 nm** and a bed temperature of **95ºC**.

Increasing N_2 inlet pressure and evaluating its impact on perovskite coat morphology with the prototype chamber

Objective: To investigate effects of varying N_2 pressure on coat morphology (surface roughness)

N_2 flow inlet pressures were increased from 5 psig to 25 psig while the 25 wt % perovskite precursor solution of MAI + PbI_2 in DMF was coated at 95°C and 150 cm/min bed speed. At 5 psig, the surface roughness reduced to **43 nm** on the right portion of the film and **44 nm** on the left portion of the film. The film remained unchanged till 15 psig,

after which it had a significantly thinner and smoother coat at 25 psig and 120 cm/min. The coat quality stood apart in terms of morphological appearance. The surface roughness of this coat was **49 nm** at the right portion. The surface roughness of the left portion could not be calculated because of valleys created by the flowing N_2 over the coat layer, resulting in excessive noise. 40 wt % perovskite solution was prepared and was coated on PET substrates. It was observed that the film coated at 10 psig qualified as an acceptable coat because of the higher solute concentration of MAI and PbI_2 crystals. At this concentration it was also observed that only coating speeds greater than 150 cm/min results in a coat with a desirable surface roughness.

Image analysis:

A stagnation point at the N_2 flow-bed zone leads to the development of a low-pressure zone. This guides the N_2 flow over the active layer during the coating process. Due to a recirculation zone at the top area seen in Figure 17, there is a balance between both zones. This can be seen from the coated strips by means of variation in the location of a black patch that extends across the length of the film. The location of the patch kept moving to the left, against the direction of the flowing N_2 with a gradual decrease in the patch width. These experiments show that when the pressure was ramped upto 25 psig, the black patch (dark region) shifted to the left (5 psig) till it disappeared (25 psig). The scattering of drops can be avoided by iterating the N_2 flow (17-23) psig with the bed coating speed with added alterations in the design of the chamber.

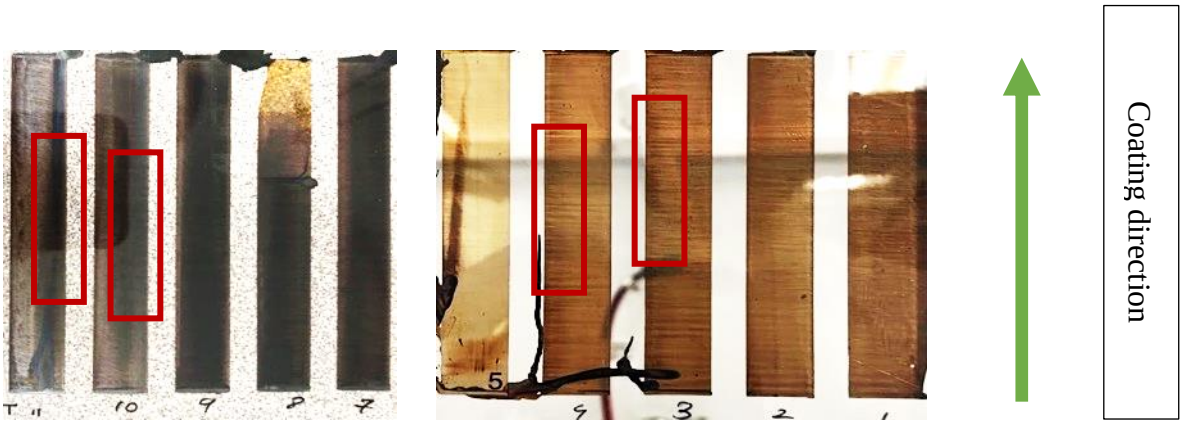

Figure 29 a) Highlighted dark regions to the right when coated at 3 psig b) Highlighted dark regions to the left when coated at varying inlet pressure, fixed temperature

Establishing pristine perovskite films with and without N_2 flow with the prototype chamber

Objective: Determine coating speed and create cases for comparison with and without N_2 flow

The 25 wt % perovskite precursor solution was coated on PET substrates with a bed temperature of 95ºC and speeds of 150 cm/min, 140 cm/min, and 120 cm/min. 5 films were coated in ambient, while the other 5 films were coated in the presence of nitrogen flow at the coating head. The films were not annealed. The sub-objectives of this experiment are to study the effect of N_2 on the perovskite microstructure and also compare annealing behavior of the films in the following experiment.

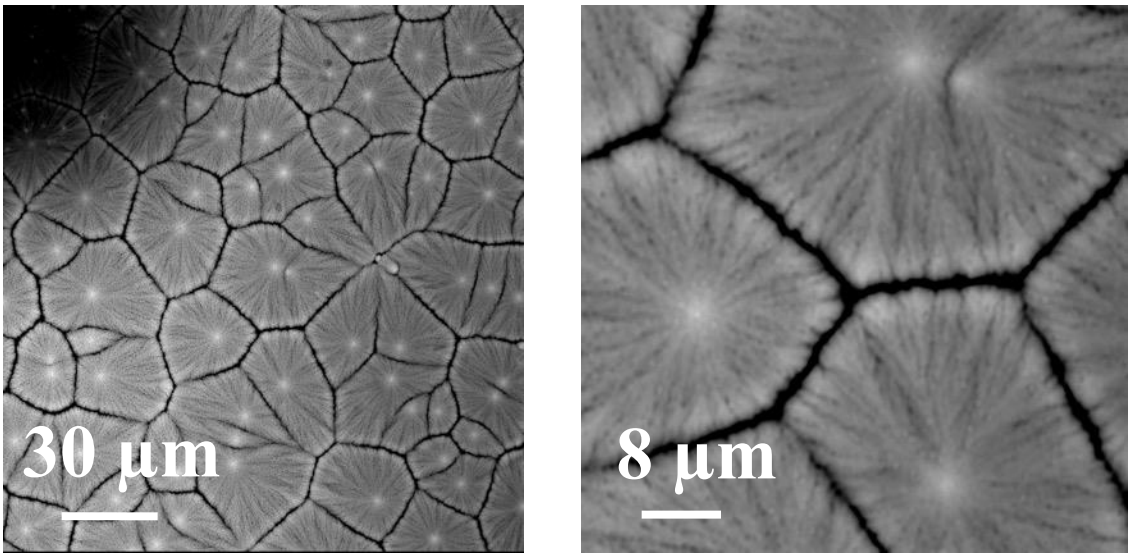

Figure 30 Pristine perovskite films at 150 cm/min

Ink printing parameters for perovskite:

Temperature (°C)	Speed (cm/min)	Pump rate (µL/min)	N_2
95	150	45	No flow
95	150	45	5 psig, 10 psig, 15 psig

Table 5 Perovskite printing parameters

Effect on annealing times on the films coated on the presence of N_2 flow with the prototype chamber

Objective: Studying impact of annealing times on perovskite films coated in the presence of N_2 flow with the prototype chamber

An N_2 flow pressure of 8 psig was chosen while printing the perovskite precursor solution on the plastic substrates. The speed was kept constant at 150 cm/min. The experiment consisted of time samplings ranging from 30s-60 min. The films were then characterized under the OLS4100 laser microscope and the Phenom Pro X SEM. Thermal annealing is necessary to quench photoluminescence in perovskite solar cells as it enhances the charge transport of carriers in the vertical direction directly relating to photovoltaic performance. A higher annealing time can induce thermal decomposition in perovskite materials and under annealed films suffer from insufficient charge transport [61]. When compared with the SEM images of the pristine perovskite images, the grains appeared to have not maturely formed and instead developed into a structure with a spherical morphology. The film has a lacunose morphology but nevertheless displays a uniform spread with higher densities.

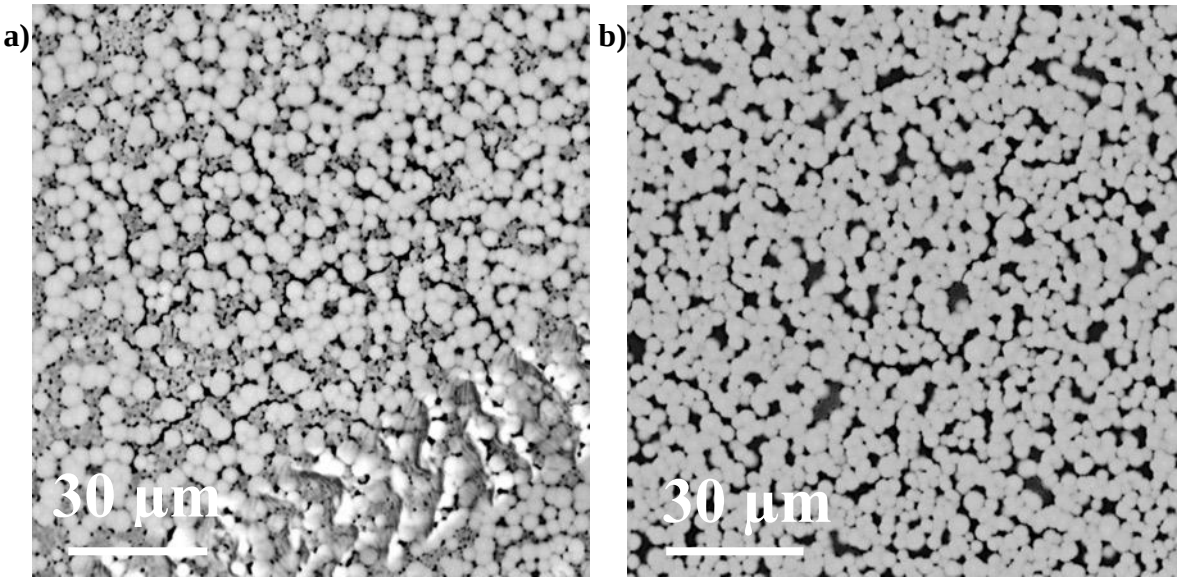

Figure 31 Perovskite precursor solution coated in the presence of N_2 a) Annealed for 60 min. b) Annealed for 30 min.

Image analysis:

These structures were eliminated from films that were coated in the presence of the new environmental chamber and were replaced by grains in the size range of 5-15 um, which has been explained in detail in the proceeding experiment. The following are the possible reasons for incomplete grain formation:

- The location of the air-knife is critically close to the coating head, resulting in an instant drop in temperature of the substrate at that location from 95°C to ambient (25°C), this temperature drop hinders the formation of nucleation sites and curbs the growth of grains
- Due to close proximity of the flowing N_2 to the coating head, the DMF solvent vapors are instantly removed resulting in a dry film within seconds. The dry film cannot promote any grain formation.
- The N_2 flow caused a spike in the evaporation rate, resulting in less or minimal grain growth with many nucleation sites.

Experiments with new large-area environmental chamber

Objective: To investigate the use of the final environmental chamber with perovskite printing and study the effect of varying N_2 flows on the perovskite microstructure and morphology with and without varying annealing times.

The precursor solution used is a 25 wt % solution as used in earlier experiments. The air-knife in this experiment was set at 90°, such that the mouth of the air-knife pointed vertically downwards instead of directly facing the perovskite layer. The N_2 after flowing downwards fills the chamber after which a meniscus is created with the substrate and coating is executed. Coating was done at a bed speed of 150 cm/min with N_2 flow successively increasing from 10 psig to 30 psig. The first five coats are not post-annealed. Films that were printed at 30 psig N_2 flow was annealed on the sheet-coater bed in an N_2 environment for 20 min, 10 min and 5 min, to compare the variation in grain size and morphology with varying annealing times. Franeker et al. showed in an SEM image of

annealed perovskite films that the grain size grows with increase in annealing times as we will see in later experiments [61].

No annealing:

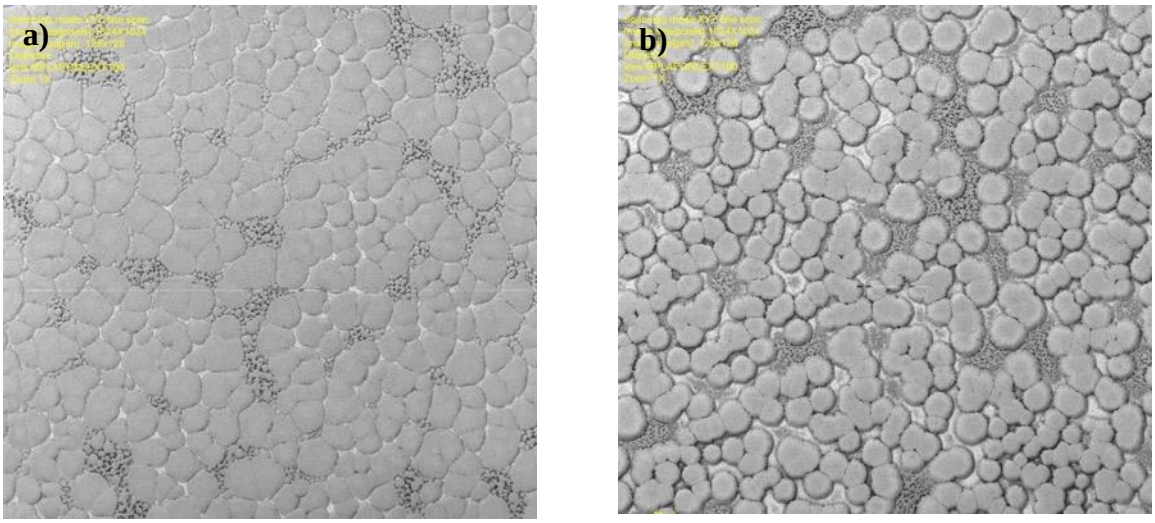

Figure 32 a) Film printed at 10 psig N_2 flow. b) Film printed at 30 psig N_2 flow.

Image analysis: The packing density of grains in the film printed at 10 psig is high with narrow grain boundaries and flatter grains with uniform size distribution. There are only few areas of incipient grain formation which can be avoided either by using a higher N_2 flow or altering printing parameters. The average surface roughness for this film is **54 nm.** In the image on the extreme right, the grains appear to have a spherical structure implying slight vertical growth of grains, leading to wide grain boundaries, inhomogeneous grain distribution and more areas of incipient grain formation. The average surface roughness measured for this film is **120 nm.** Increase in the N_2 flow rate leads to a faster evaporation rate, thus minimizing linear grain growth and contributing to vertical growth in grains leading to rougher film morphology. An appropriate N_2 flow pressure for printing solutions falls in the range of 10 psig-20 psig, with lower flow values leading to a slower evaporation rate and higher flow values accelerating the evaporation rate.

Annealed films: The size of grains typically increases with increase in the annealing times as evidenced in experiments that were carried out in the following sections. In this case,

the grain sizes of the developed grains changed slightly after a 20 min annealing time. It is interesting to note that the incipient grain zones transformed into mature grains of smaller sizes in the range of 1-3 μm, although grain density and grain boundaries have remained unchanged.

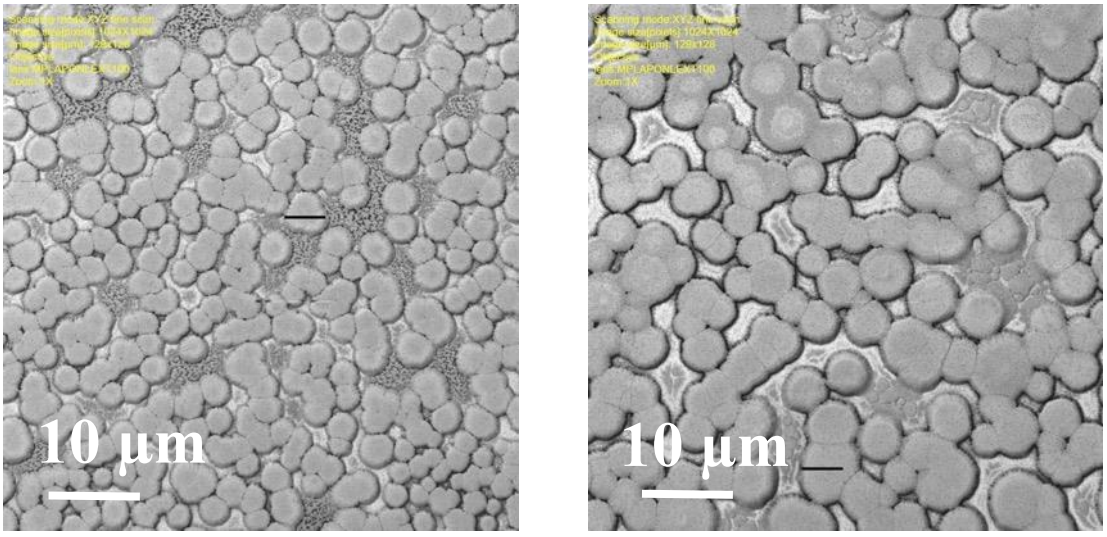

Figure 33 Films annealed for 20 min with smaller grain sizes

Comparison between films printed in the presence and absence of N_2 flow

Objective: To analyze the differences in the perovskite morphology and grain structure in both cases for films annealed for variable durations.

In this experiment, the perovskite precursor solution is printed at 95°C and a bed speed of 150 cm/min and are annealed successively for 5 min, 10 min and 20 min. When the grain sizes for annealed films were compared for the pristine perovskite case, an increasing trend in the grain sizes, surface roughness and film thickness with increasing annealing times is observed. In the successive experiment, the perovskite precursor solution was printed with the same parameters in the presence of nitrogen at 15 psig inlet pressure with the air-knife tilted at 45°. Annealing was done in the presence of N_2 flow for 5 min, 10 min and 20 min with the programmable bed moved at 50 cm/min within the chamber towards the air-knife.

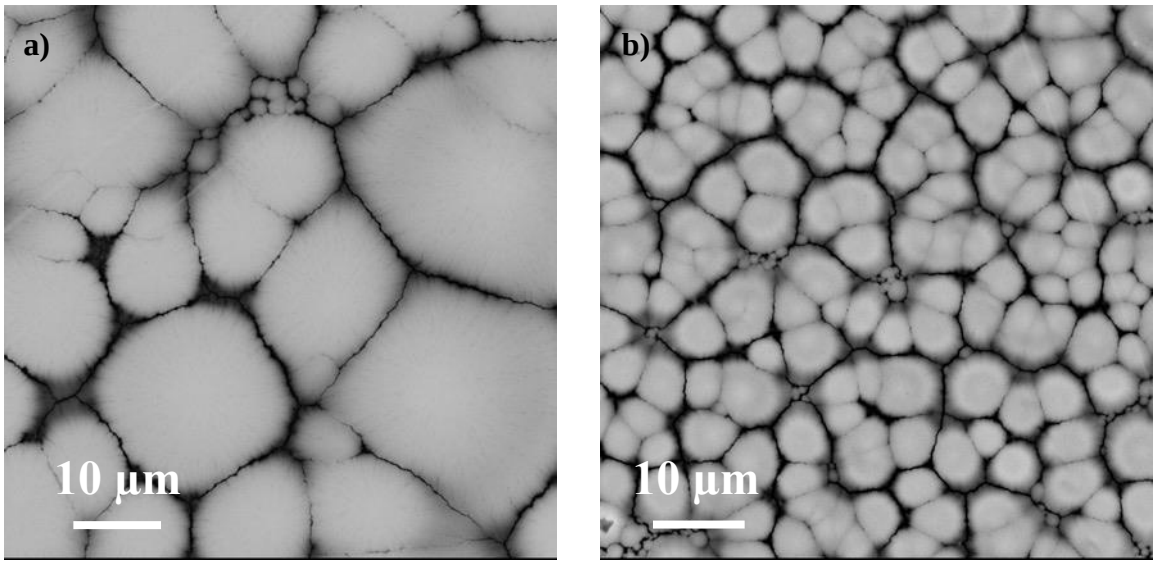

Figure 34 SEM images: a) Perovskite film printed in the absence of N_2; b) Perovskite film printed in the presence of N_2 in the tilted air-knife experiment

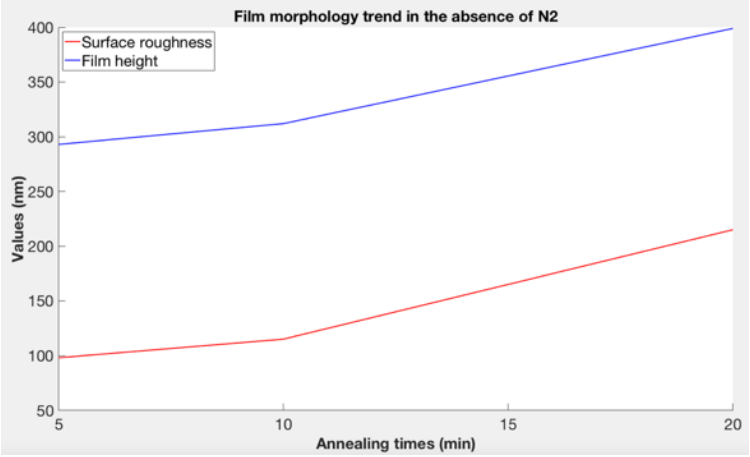

Figure 35 Trends of film morphology for pristine perovskite films.

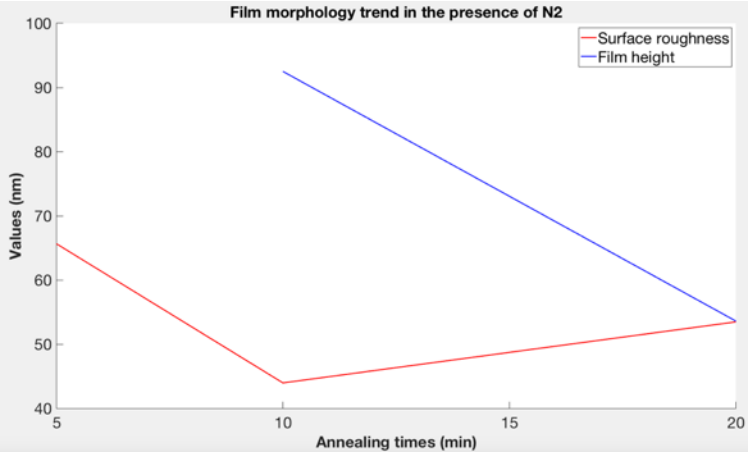

Figure 36 Trends of film microstructures for films printed in the presence of N_2 flow

Image analysis: The average size of the grains reduced by 52% for the films annealed for 20 min, 63.6% for the films annealed for 10 min and 35.4% for the films annealed for 5 min. This is an indication of change in the evaporation rate induced by flowing N_2. As seen earlier, the N_2 increases the evaporation rate leading to increased nucleation and lesser grain growth. A 15 psig inlet pressure does not contribute to vertical grain growth, but instead smoothens out the printed layer and pushes the solute to the meniscus, promoting faster grain growth [55]. The overall surface roughness of the films has also reduced from 98 nm, 115 nm and 215 nm for the 5 min, 10 min and 20 min annealed cases to 65.66 nm, 44 nm and 53.5 nm respectively. The inconsistencies in the surface roughness values maybe because of:

- Ridges formed on the surface of the films due to flowing N_2
- Intermittent interaction between annealing and flowing N_2 controlling the film microstructure when the bed is moved during annealing. There is a general trend of increasing surface roughness with increasing annealing time as seen in Figure 35 and reduced surface roughness with N_2 flow.

The thickness of the film was also measured in both cases for all films annealed for varying times and it was measured to reduce by 345 nm & 219 nm for 20 min and 10 min cases respectively.

Slow-speed perovskite coating in the presence and absence of N_2 flow with the large-area chamber

Objective: To investigate coating with bed speeds as low as 10 cm/min

The 25 wt % perovskite precursor solution was coated at slow speeds of 10 cm/min with a pump rate of 15 µl/min. Slower coating speed is expected to promote grain growth by allowing faster solvent evaporation. The resulting coat is a lustrous, brown perovskite film with higher optical clarity and high coat quality in terms of morphology with no pinholes and high surface smoothness. Pristine as well as N_2 coated films are annealed for 5 min and 10 min in a nitrogen atmosphere.

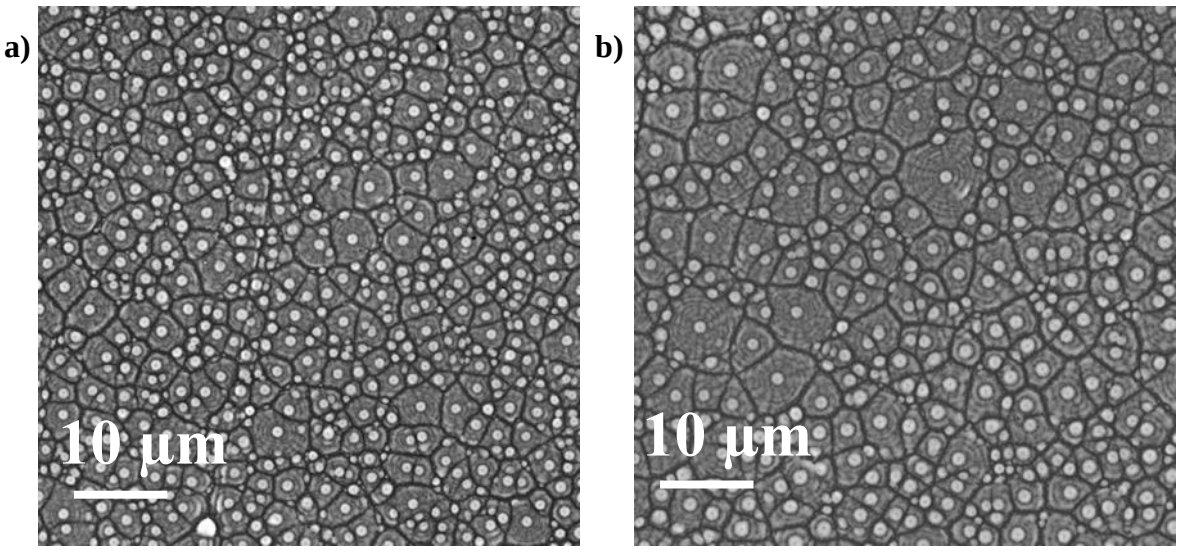

Figure 37 SEM images: a) Perovskite film printed in the absence of N_2; b) Perovskite film printed in the presence of N_2

Image analysis: As observed in the SEM images, the grain sizes of the perovskite printed in the presence of N_2 increased from 4.9 µm, 4.6 µm and 7.9 µm to 9.3 µm, 6.32 µm and 9.83 µm for 10 min, 5 min and non-annealed films from the pristine case which is directly opposite to that of the pristine perovskite case. When compared with the images from higher coating speeds, it can be inferred that the grains from the slower coating process are highly packed with narrow grain boundaries and visible nucleation sites. The grains are flat and lack a spherical shape unlike SEM images from Figure 34. As bigger grains are related to increasing surface roughness [62,63,64], the surface roughness of N_2 films are insignificantly higher than that of pristine films.

Through these experiments it is inferred that the film morphology and grain microstructures can be regulated by constrained nitrogen flow and altering the sheet coater parameters in conjunction with the solution system used.

7. Additives in Perovskites

7.1 Varying concentrations of additive: Chloronaphthalene

To improve the morphology of as-cast perovskite films, Chloronaphthalene (CN) was added in the solution of MAI + PbI_2. CN is used as an additive in perovskite printing to improve the morphology of crystals formed and to aid in the regulation of the crystallization kinetics of perovskite films [37]. The cast films were lustrous, pinhole free and had a homogeneous surface coverage than pristine perovskite films. It was also observed that the films printed with CN converted much faster than additive-free perovskite. As CN has a much higher boiling point (259°C) than DMF (153°C), CN molecules get retained in the film till it has dried, ensuring good control over resulting high quality perovskite crystal formation. It has been observed that the crystallization rate of perovskite crystals is effectively influenced by this additive [37]. Being an aromatic compound, the naphthalene ring in CN regulates crystallization kinetics due to its strong steric effects. In a series of experiments conducted by adding 20 µl of CN in 25 wt % perovskite precursor solution (1 wt % CN), we see that the coatings had less dense perovskite crystal coverage with uneven grain distribution. The coats were dark gray in color with slow conversion rates. The coatings were done at 85°C and the bed speed was varied from 120 cm/min to 180 cm/min in the presence of N_2 flow with inlet pressures varying from 10 psig to 25 psig. It is concluded that when CN is added as an additive in the perovskite solution, the coating speed must be brought down to 50 cm/min and the pump rate must be adjusted to dispense 45 µl/min. The coating temperature of 95°C that was selected for pristine perovskite solutions worked well with CN additives resulting in the best coat with crystalline homogeneity, with no intermediate dark or light regions on the film surface.

Alteration to the N_2 flow chamber must be done in order to achieve good coats for this additive based perovskite precursor system as coating in the presence of 10 psig N_2 for CN added films did not give desirable results.

Study of varying additive concentrations and its impact on perovskite morphology with varying annealing times

CN was added in the 25 wt % perovskite precursor solution in the varying concentrations of 1wt %, 3 wt %, 5 wt %, 10 wt % and were coated on PET substrates. Three films were annealed for 20 min, 10 min, 5 min at 95°C each and one was air-dried at 25°C with no annealing time.

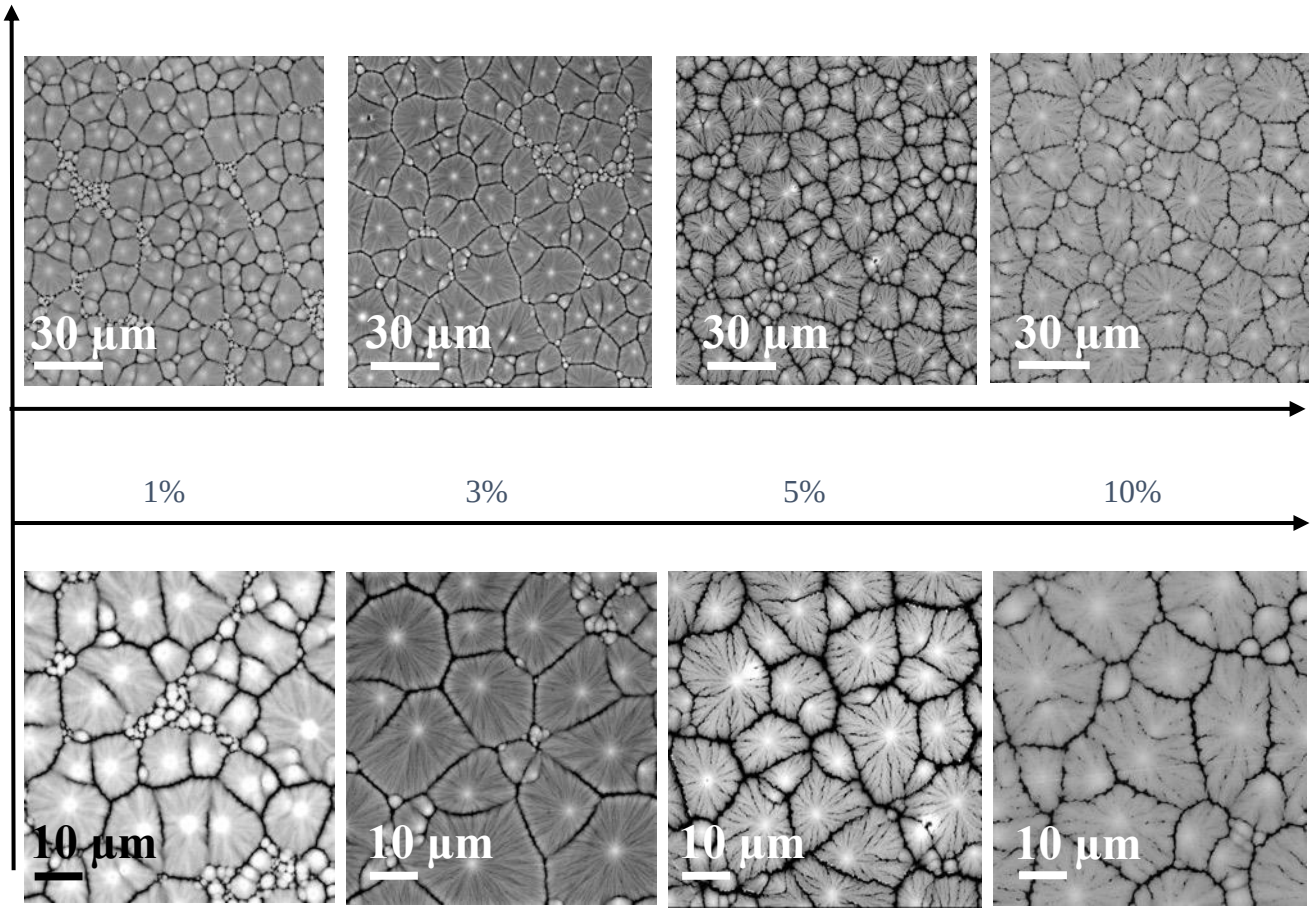

Figure 38 Varying CN% with constant annealing time of 10 min

7.2 Absorbance and annealing time

Based on the bathochromic shift observed in films with the CN additive, Song et al. observed that the CN plays a role in increasing light absorption by developing better crystal structures and partly due to improved surface coverage of the active layer [37].

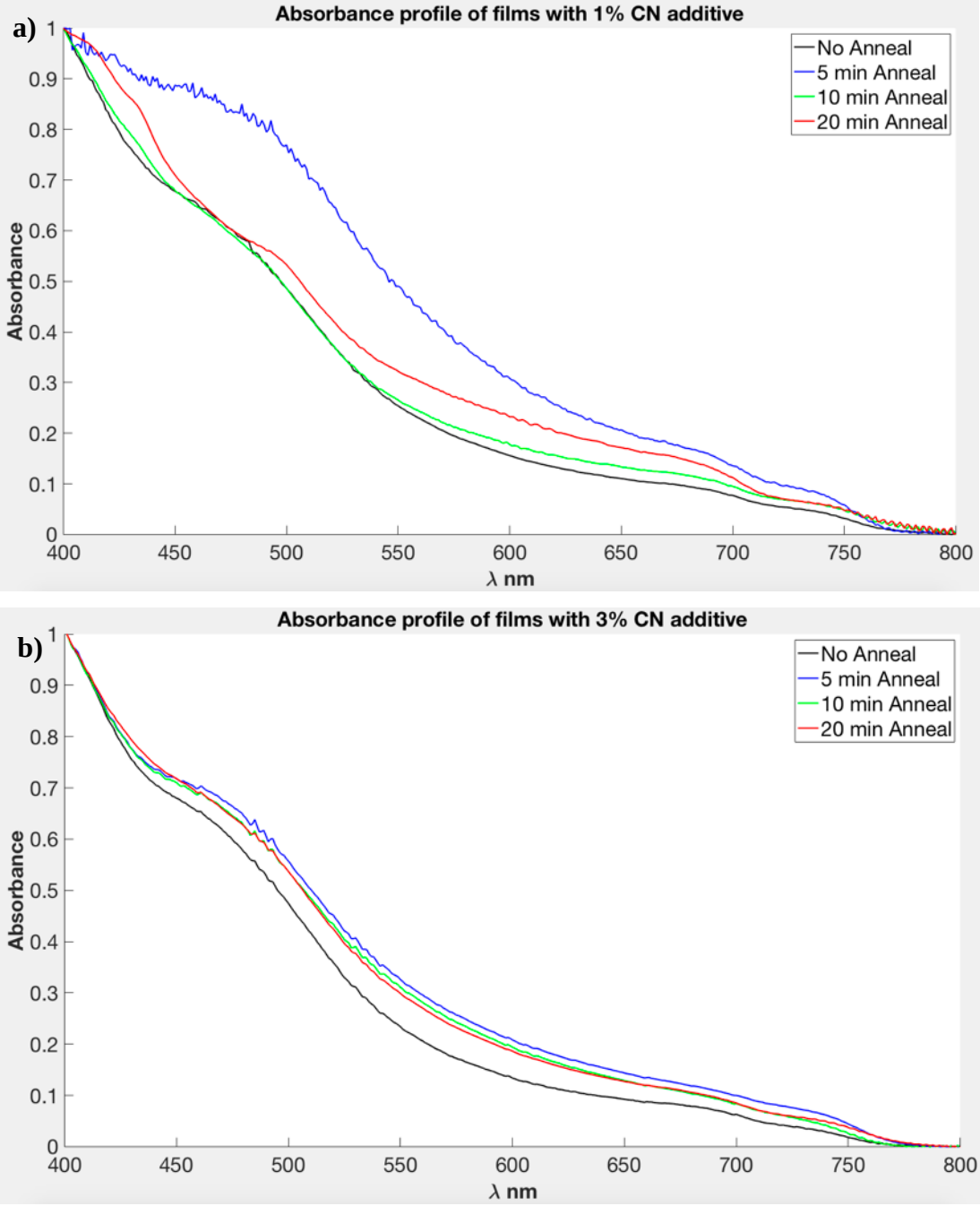

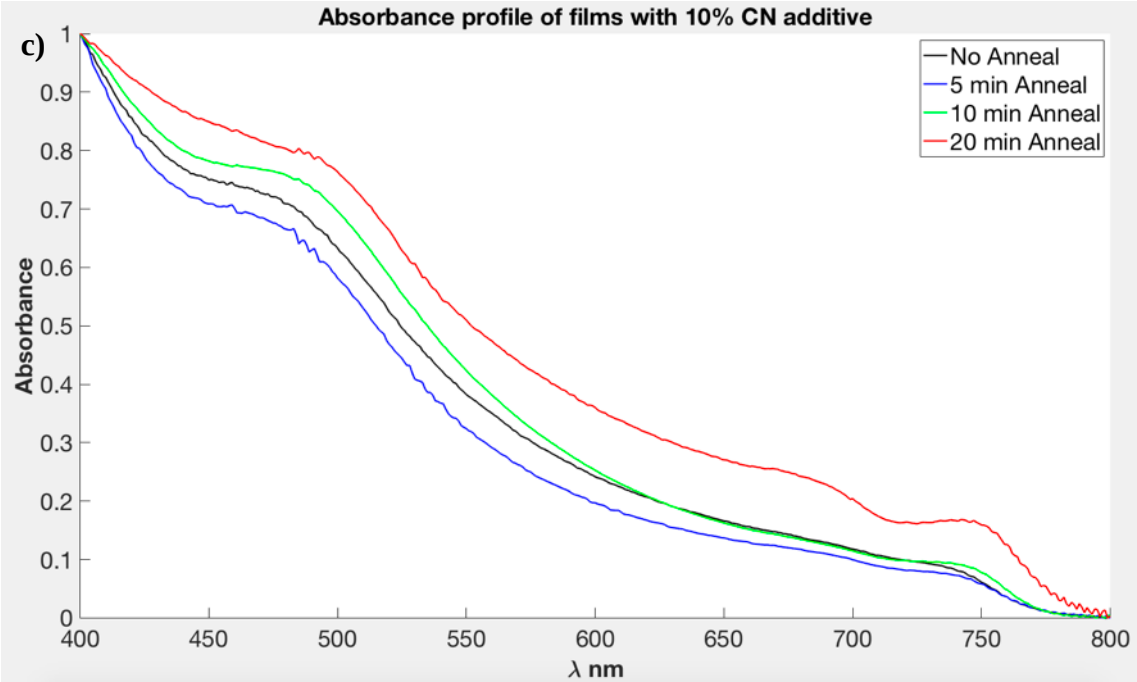

Figure 39 a) UV absorption profile for 1% CN additive b) UV absorption profile for 3% CN additive c) UV absorption profile

Observations: The films that were coated with 3 wt % and 10 wt % CN additive had a similar morphology, with the 3 wt % CN films developing lesser pinholes and dewetting sites. The films were measured for light absorbance in the 400-800 nm range and it was seen that the 20 min annealed films absorbed lesser than the films annealed for 10 min and 5 min for both 3 wt % CN and 10 wt % CN cases. This is possibly due to a degradation mechanism that is induced in the films when annealed for 10 min or greater. Films deposited with the 10 wt % CN added precursor solution developed grains in the order of 10 µm-20 µm. The film annealed for 10 min had the largest grain size of 20 µm. When a 3 wt % CN added solution was coated, the grains sizes fell in the range of 15 µm-30 µm. The film annealed for 10 min had a similar grain size of 20 µm. Large closely packed grains are desired for efficient charge transport, thus positively influencing the power conversion efficiency. The microstructure of the films coated with 3% CN additive revealed uniform grains that formed around the nucleation site in a highly ordered radial pattern with smooth grain edges. The films coated with 10 wt % CN added solution had grains with rough edges and cracks along its lengths but with narrower grain boundaries.

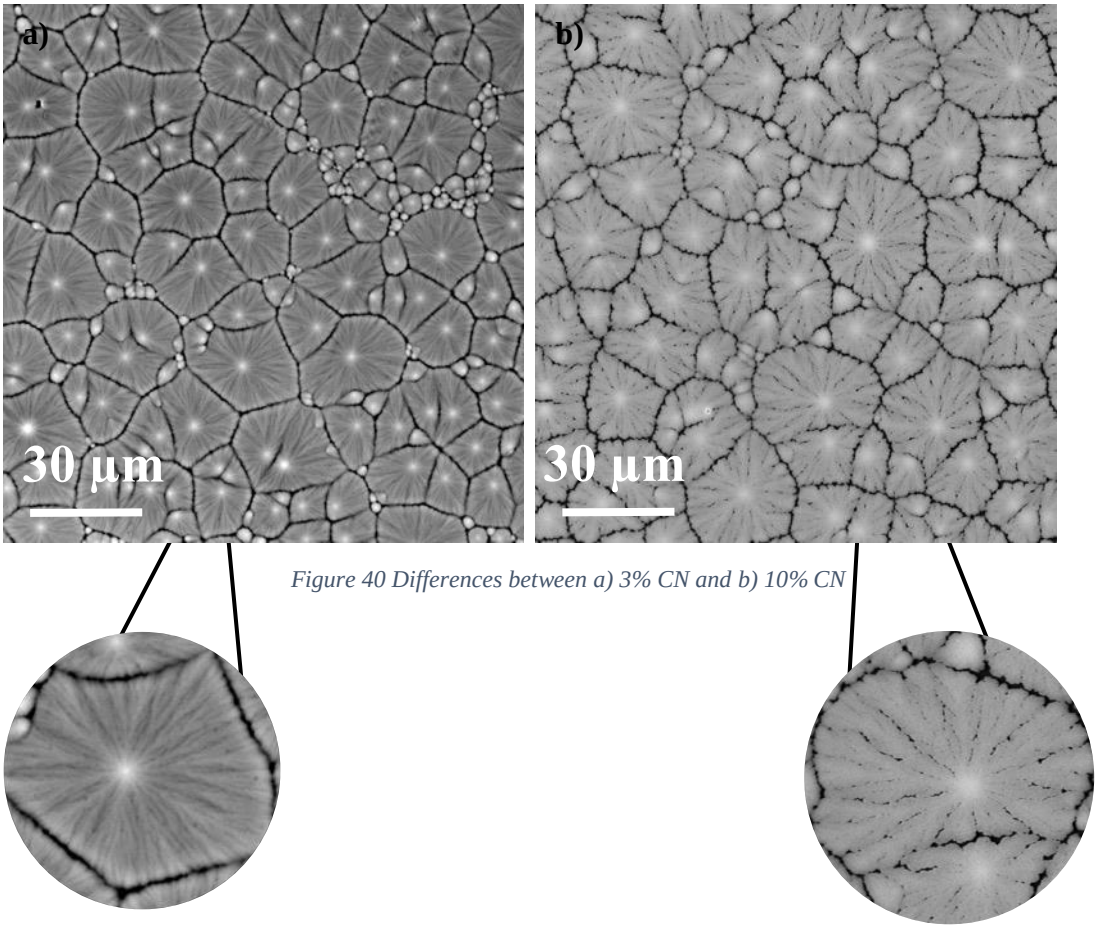

Figure 40 Differences between a) 3% CN and b) 10% CN

A highly packed grain system with narrow grain boundaries could be the explanation for higher absorbance. A better surface coverage and absence of pinholes is another explanation for measured higher absorbance [65]. The 10% CN, 10 min films show a higher absorbance than the films annealed for 20 min and 10 min for all other additive cases. The 3% additive case looks the best based on the grain distribution and roughness values. Higher roughness values could also contribute to a higher absorbance profile as evidenced for the 10% CN case as seen in Figure 41, but a higher roughness can lead to shorting or shunting within the device, thus the 3% additive case is recommended.

Annealing time (min)	1%	3%	10%
20	24.3	9	15.5
10	12.5	7	26
5	15.1	15.33	38
No anneal	13.32	9.66	35

Table 6 Surface roughness values in nm for varying additive concentrations

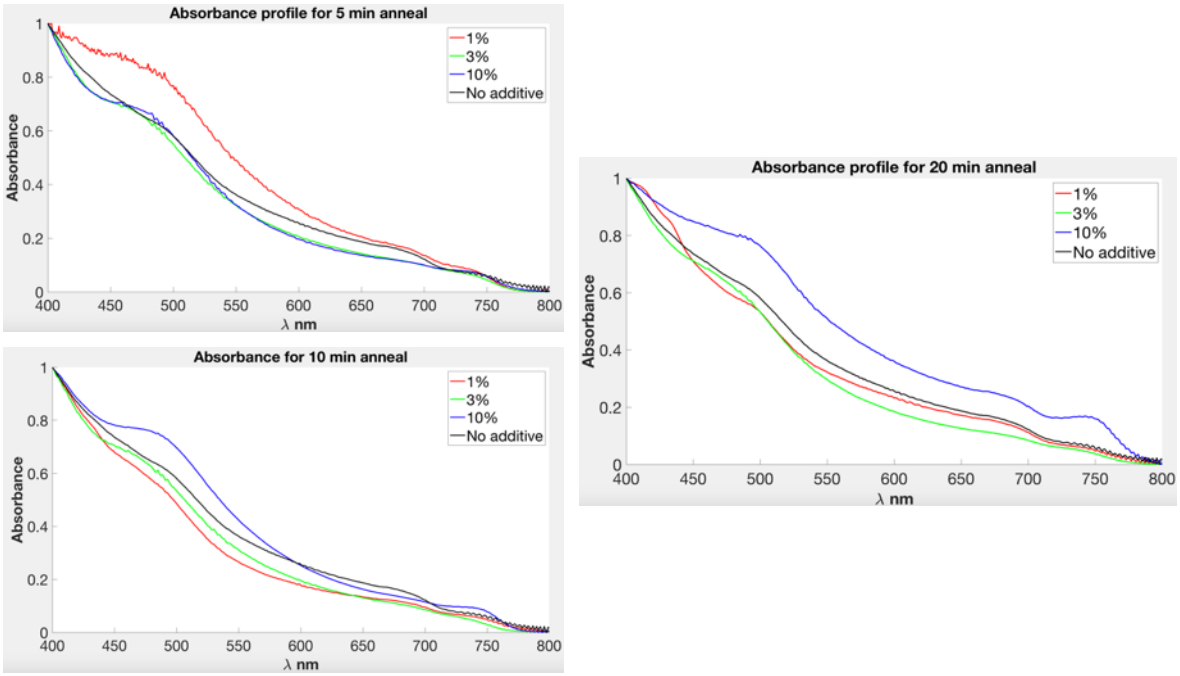

Figure 41 Absorbance profile for CN added films at different annealing times

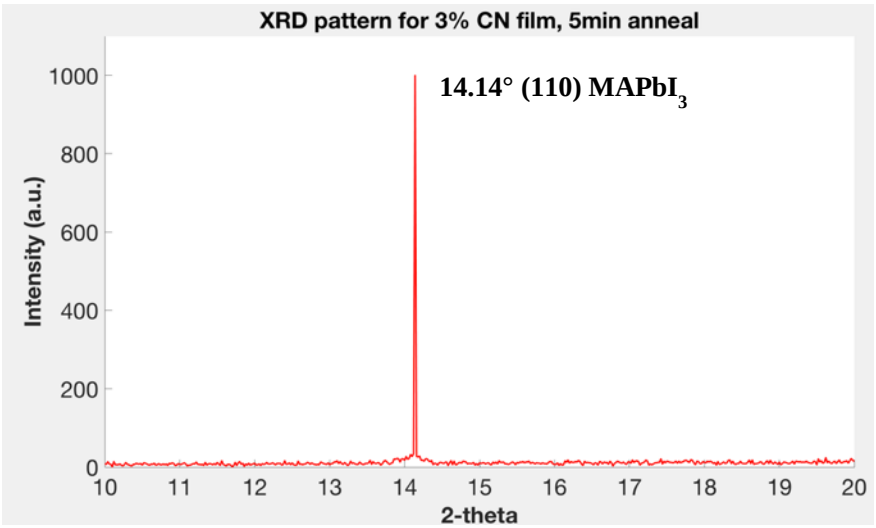

Figure 42 XRD pattern for 3% CN added films and annealed for 5 min

7.3 Coating with Anisoles (4-tert-butylanisole)

To employ a less hazardous and non-toxic additive option as compared to the CN, another miscible high boiling point (222°C) antisolvent, 4-tert-butylanisole (tbA) was used. Similar to the case of CN in the earlier section, the kinetic traces as measured by Paek et al. show that antisolvent additives typically contribute to a higher absorbance profile implying a faster nucleation growth and grain formation leading to pinhole free films with increased electrical performance [66].

Recipe followed for further experiments

DMF=4 ml
DMSO (Dimethyl Sulfoxide) =314 μl
MAI=705 mg
PBI2=2044 mg
tbA (4-tertbutyl anisole) =130 μl

Slow-speed coating in the presence and absence of N_2 flow

Objective: To investigate coating with bed speeds as low as 10 cm/min for the anisole system

The anisole added perovskite solution was coated at 95°C, 10 cm/min in the absence of N_2 initially, after which flow was resumed at inlet pressures of 10 psig, 15 psig, 20 psig and coating was executed. The resulting films are analyzed for variation in surface roughness and grain sizes. The coat printed in the absence of N_2 flow had an average roughness of 34.7 nm and the coat printed under the influence of N_2 flow was measured to be 2.9 nm rougher. This roughness can be attributed to the 20 μm increase in grain size in the films printed with N_2 flow.

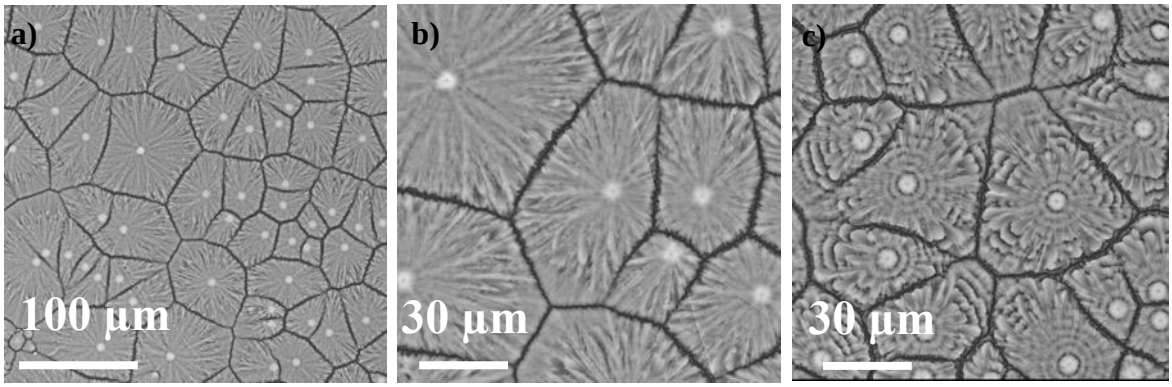

Figure 43 SEM images: a) and b) Grain microstructure for film printed in the presence of N_2 flow c) Grain microstructure for the film printed in the absence of N_2 flow

Image analysis: It is seen in the additive-free experiments that slow-coating speeds typically contribute to a reduced grain size in the micrometer scale in the range of 3-8 µm. Therefore, the increase in the grain size to the range of 60-80 µm and the reduction in the width of grain boundaries can be attributed to the addition of tbA. It can be validated that the growth kinetics of crystals has significantly improved in this case. It is seen that the introduction of N_2 flow has altered the grain morphology leading to a finer and linear growth from the nucleation site.

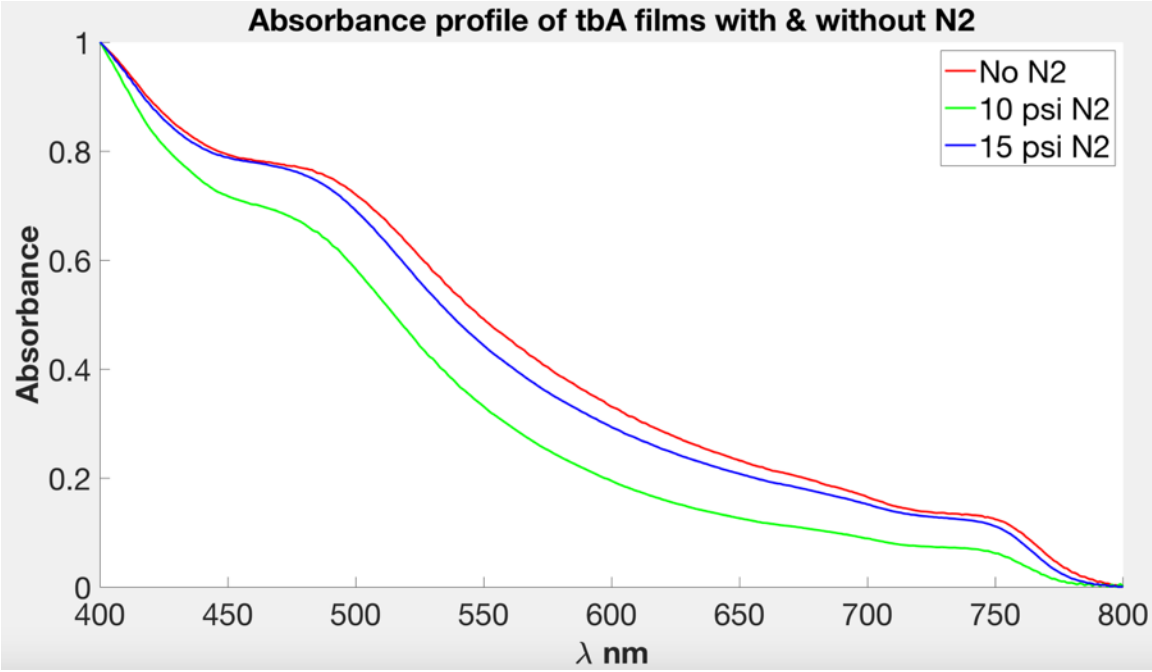

Figure 44 UV absorbance profile of films printed in the absence of N_2, 10 psig and 15 psig

The absorbance profile indicates that the film printed in the presence of 15 psig N_2 absorbs close to the perovskite film printed in the absence of N_2. Due the presence of ridges created by flowing N_2 over the printed film, there is inherent light scattering which probably caused a lower absorbance despite the larger grains. The presence of Photoluminescence (PL) indicates that the excitons haven't recombined and that these perovskite crystals are free from morphological defects [67], [68].

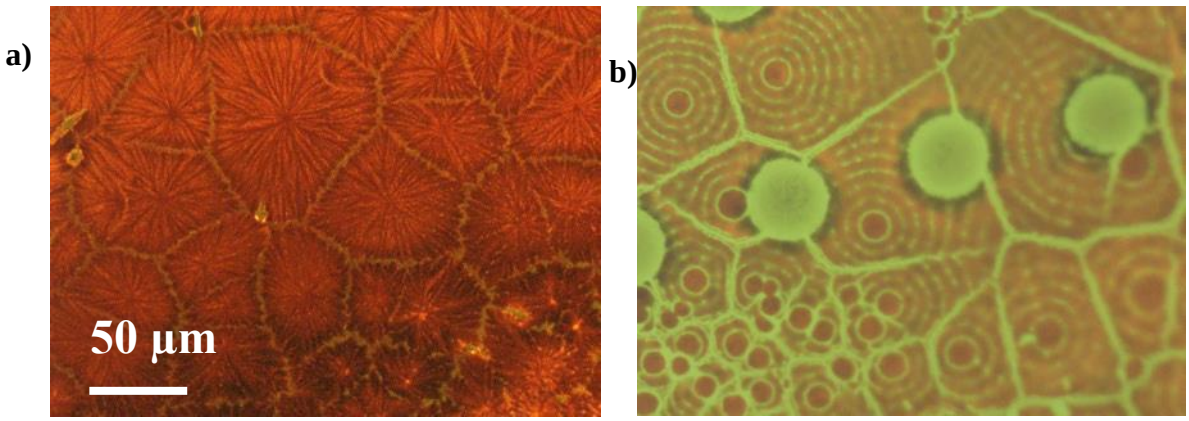

Figure 45 PL image of films with a) 4-tertbutyl anisole b) Coated on copper dots

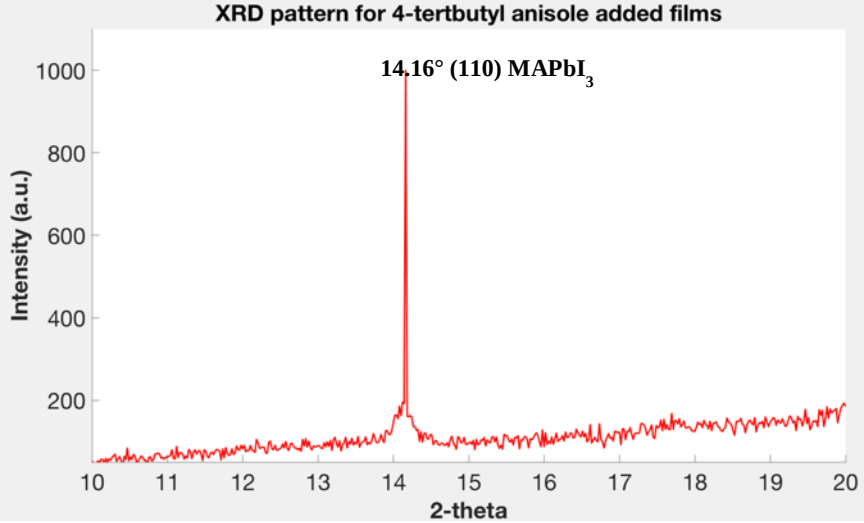

Figure 46 XRD pattern for 4-tertbutyl anisole added films

Coating in varying relative humidity

Objective: To investigate anisole coating in varying relative humidity

To analyze the effect of humidity and determine an appropriate humidity for printing perovskite precursor solutions with 4-tertbutyl anisole as the additive, films were coated in a relative humidity of 10%, 20%, 30%, 40% and 60% and 21.1°C at a bed temperature of 95°C and a bed speed of 10 cm/min.

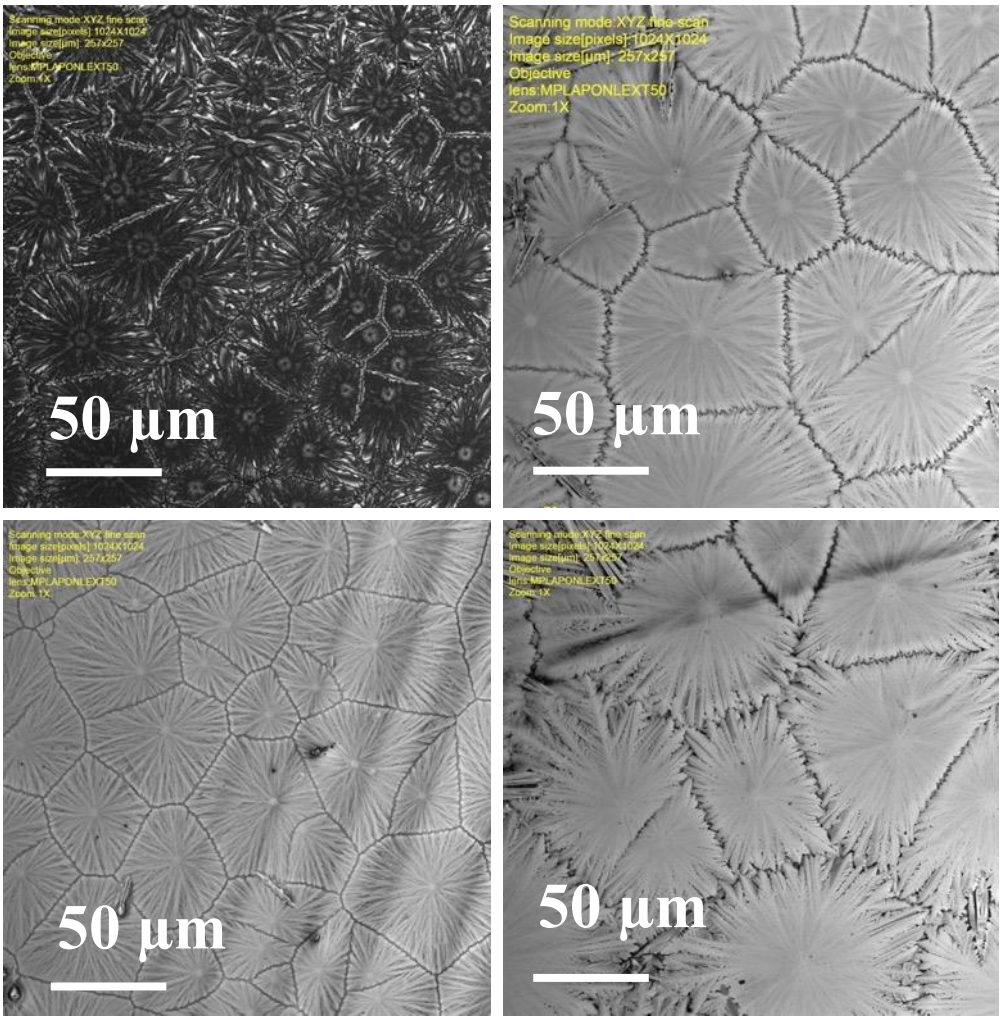

Figure 47 a) 10% RH b)20% RH c) 30% RH d) 60% RH

RH	10%	20%	30%	40%	60%
Surface roughness (nm)	61.2	44	10.8	47	76

Table 7 Varying surface roughness values with varying relative humidity

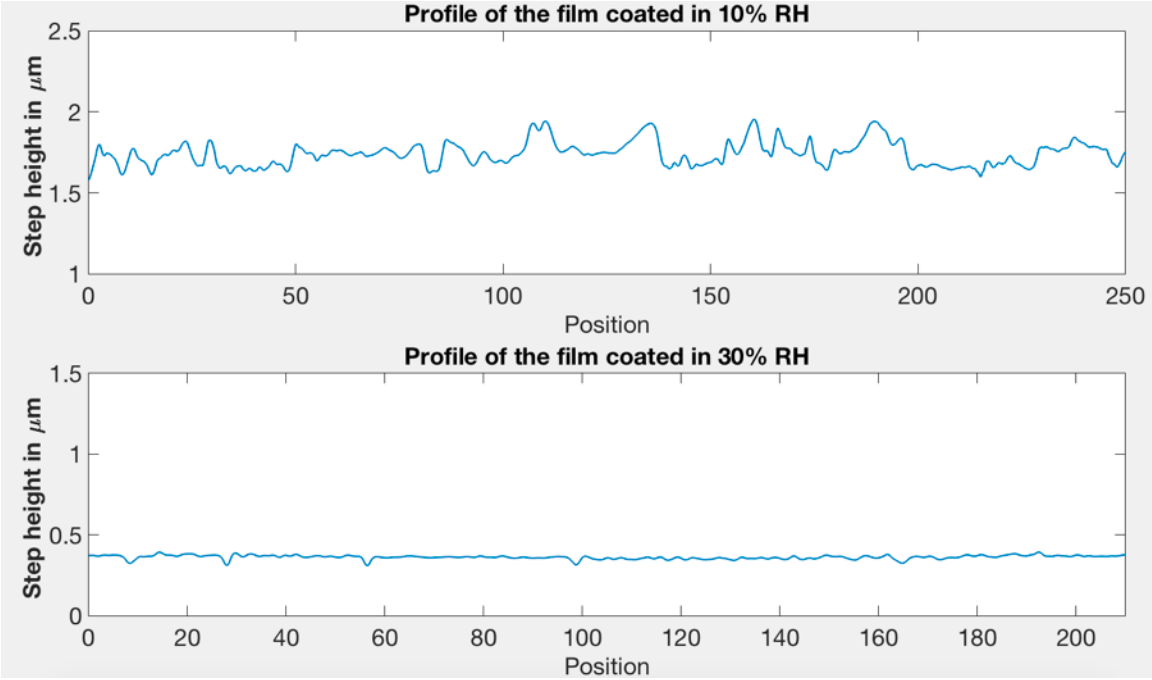

Figure 48 Roughness profile of the films coated in 10% RH and 30% RH

It is seen that the film printed in RH 30% was measured to be the smoothest film. The SEM images reveal that the grain microstructure is underdeveloped (10%) with rough grain edges (20%) and overdeveloped grains with cracks extending from the nucleation site overlapping onto adjacent grains (60%) which are responsible for highly rough films. It can be concluded that for the tbA additive, coating in ambient (RH 30%-RH 35%) results in films with best results in terms of coat morphology and grain microstructure.

8. Conclusion

The work presented in this thesis on slot-die coated perovskite solar cells explores the role of introducing of a processing step during fabrication. In addition to this, it focuses on the scale-up of the printing process for the perovskite active layer from a maximum of 1 cm^2 active area fabricated on the spin-coater to a length of 10-43 cm long print lines on the sheet-coater, directly transferrable to the commercial scale roll-to-roll printer [69]

The avenue of using a slot-die coater is a relatively novel approach in the field of material science and solar energy. Thus, experiments are conducted to arrive at optimal print parameters to assure outstanding print quality that is comparable to high efficiency devices fabricated on the spin-coater. It is inferred that a change in any one of the parameters influences the print to a major degree. In achieving desirable homogeneous, uniform, and pinhole free coatings, this thesis also presents work done towards the perovskite precursor solution development. A range of solutions were formulated and coated after which advanced spectroscopy and microscopy techniques are conducted on the films to evaluate the microstructure and morphology of the coated layer.

Throughout the duration of the project, printing parameters on the slot-die coater are established for NiO_x nanoparticles HTL, perovskite solution, and the additive based perovskite solution. A study on printing conditions are also carried out by utilizing the control room at the testbeds to vary humidity and temperature.

To investigate the addition of high boiling point antisolvents in perovskites, Chloronaphthalene is added in varying concentrations and its effect on the crystallization kinetics is studied with respect to annealing times. A less toxic and safer alternative, 4-tertbutyl anisole is also used as an additive. Large micrometer sized grains with high packing density and smooth film profile are achieved by using this additive. A device based on this precursor solution falls in the future work for this thesis.

The NiO_x printing parameters for the slot-die coater are fixed at 65°C, 120 cm/min for uniform, aggregate free coatings with an average surface roughness of 5 nm. The particle sizes must stay within the 12-13 nm range to ensure such smooth coatings. It is determined that to implement the use of an air-knife setup and also achieve perovskite grain formation, the location of the air-knife must not be critically close to the coating head. The perovskite printing parameters were fixed at a coating temperature of 95°C and 10 cm/min or 95°C and 150 cm/min with pump rates varying from 15-45 μl/min in an RH of 30-40%.

A distance of less than 2" from the coating head resulted in incomplete grain formation, whereas a distance of greater than 10" led to fully-formed grains. At a high coating speed of 150 cm/min and a coating temperature of 95°C, the grain sizes of films coted in the presence of nitrogen were reduced in comparison to the case in open-air. At the same temperature, but a slow-coating speed of 10 cm/min resulted in bigger grains in the case of nitrogen. It is concluded that the grain sizes can be controlled with a nitrogen flow of 15 psig. Using different flows resulted in similar trends but with ridges formed over the film surface for nitrogen inlet pressures greater than 15 psig. In addition to controllable grain sizes, the surface roughness and film height also followed a decreasing trend for films printed in the presence of nitrogen. The surface roughness reduced by about 70 nm and the film height by about 200 nm. Thus, the air-knife setup can be used accordingly with a maximum inlet pressure of 15 psig to achieve desirable grain sizes with narrow grain boundaries and surface profile by influencing the drying rate by fast solvent evaporation by means of a recirculation zone within the chamber.

In case of high-temperature boiling point antisolvents, addition of CN resulted in pinhole-free films with a smooth texture and a higher absorbance profile. It is determined that a 3% additive concentration results in a highly packed grain orientation with best grain structures and films with a low surface roughness of about 7 nm. These films also displayed a higher absorbance profile and a 10 min annealing time is recommended for ensuring complete grain formation. When a safer and less toxic additive alternative, 4-tert

butylanisole is used, there is an improvement in the grain growth kinetics as evidenced by large grains of the order of 60-80 μm with the biggest grain sizes in the case of nitrogen assisted printing. For this anisole-based additive, printing must be done in an RH of 30-40% or ambient conditions to avoid a rough film profile, rough grain edges and overlapping grain structures.

This nitrogen flow system will be experimented with other solution-based materials to regulate film morphology and grain structures. The oxygen and moisture content within the chamber will be monitored with variations in the nitrogen inlet pressures and humidity values. Experiments with other high temperature boiling point antisolvents as additives will be carried out to investigate its effect on the perovskite solution system. A device based on this perovskite precursor solution and print conditions will be fabricated and performance parameters (PCE%, I_{sc} and J_{sc}) for the same will be tested. The long-term goal will be to translate this process to the roll-to-roll setup at the WCET.

References

1. S. Matasci, "2018 Solar Panel Cost | Updated Avg. Solar System Prices by Location," *Solar News*, 14-Jun-2018. [Online]. Available: https://news.energysage.com/how-much-does-the-average-solar-panel-installation-cost-in-the-u-s/. [Accessed: 12-Jul-2018].

2. *World Energy Outlook 2017*. Paris: OECD/IEA, 2017.

3. *Energy Flow Charts*. [Online]. Available: https://flowcharts.llnl.gov/commodities/energy. [Accessed: 12-Apr-2018].

4. "Renewable Energy," *Center for Climate and Energy Solutions*, 01-Nov-2017. [Online]. Available: https://www.c2es.org/content/renewable-energy/. [Accessed: 09-Apr-2018].

5. "Solar Energy in the United States," *Department of Energy*. [Online]. Available: https://www.energy.gov/eere/solarpoweringamerica/solar-energy-united-states. [Accessed: 07-Mar-2018].

6. "China's solar power capacity more than doubles in 2016," *Reuters*, 04-Feb-2017. [Online]. Available: https://www.reuters.com/article/us-china-solar-idUSKBN15J0G7. [Accessed: 06-Jan-2018].

7. "Recent Facts about Photovoltaics in Germany," *Fraunhofer ISE*. [Online]. Available https://www.ise.fraunhofer.de/en/publications/studies/recent-facts-about-pv-in-germany.html. [Accessed: 08-Mar-2018].

8. "Technology Roadmap," *International Energy Agency*. [Online]. Available https://www.iea.org/publications/freepublications/publication/TechnologyRoadmapSolarPhotovoltaicEnergy_2014edition.pdf. [Accessed: 06-Mar-2018].

9. J. Jean, P. R. Brown, R. L. Jaffe, T. Buonassisi, and V. Bulović, "Pathways for solar photovoltaics," *RSC Advances*, 17-Feb-2015. [Online]. Available: http://pubs.rsc.org/en/content/articlelanding/2015/ee/c4ee04073b. [Accessed: 02-Apr-2018].

10. Iakovos Tzanakis, 2006, "Combining Wind And Solar Energy To Meet Demands In The Built Environment," M.S. thesis, Mechanical Engineering, University of Strathclyde.

11. "Photovoltaic Research | NREL," *Research Team Engineers a Better Plastic-Degrading Enzyme | News | NREL*. [Online]. Available: https://www.nrel.gov/pv/. [Accessed: 12-Nov-2017].

12. L. Richardson, “Thin Film Solar Panels: Do They Make Sense? | EnergySage,” *Solar News*, 21-Mar-2018. [Online]. Available: https://news.energysage.com/thin-film-solar-panels-make-sense/. [Accessed: 22-Feb-2017].

13. First Solar’s Cells Break Efficiency Record - MIT Technology Review. Available at: https://www.technologyreview.com/s/600922/first-solars-cells-break-efficiency-record/.

14. “Why Use Gallium Arsenide Solar Cells? - Alta Devices.” [Online]. Available: https://www.altadevices.com/use-gallium-arsenide-solar-cells/,5071.1. [Accessed: 18-Feb-2018].

15. “Department of Energy,” *Department of Energy*. [Online]. Available: https://www.energy.gov/. [Accessed: 2017].

16. Cadmium Telluride | Department of Energy. Available at: https://www.energy.gov/eere/sunshot/cadmium-telluride. (Accessed: 13th March 2017)

17. CIGS Solar Cells, Simplified. Available at: http://www.solarpowerworldonline.com/2014/01/cigs-solar-cells-simplified/.

18. Wiley: Copper Zinc Tin Sulfide-Based Thin Film Solar Cells - Kentaro Ito. Available at: http://www.wiley.com/WileyCDA/WileyTitle/productCd-111843787X.html.

19. Fine tuning of the band gap in conjugated polymers via control of block copolymer sequences: The Journal of Chemical Physics: Vol 97, No 4. Available at: http://aip.scitation.org/doi/10.1063/1.463065.

20. D. Johnson, “Quantum Dot Solar Cells Break Conversion Efficiency Record,” *IEEE Spectrum: Technology, Engineering, and Science News*, 30-May-2014. [Online]. Available: https://spectrum.ieee.org/nanoclast/green-tech/solar/quantum-dot-solar-cells-break-conversion-efficiency-record. [Accessed: 06-Apr-2018].

21. Ultrathin and lightweight organic solar cells with high flexibility : Nature Communications. Available at: http://www.nature.com/articles/ncomms1772.

22. Jørgensen, M. *et al.., 2013,”* The state of organic solar cells—A meta analysis. *Sol. Energy Mater. Sol. Cells”* 119, 84–93.

23. O. A. Abdulrazzaq, V. Saini, S. Bourdo, E. Dervishi, and A. S. Biris, 2013“Organic Solar Cells: A Review of Materials, Limitations, and Possibilities for Improvement,” *Particulate Science and Technology*, vol. 31, no. 5, pp. 427–442.

24. “Perovskite Solar,” *Perovskite solar panels: introduction and market status | Perovskite-Info*. [Online]. Available: https://www.perovskite-info.com/perovskite-solar. [Accessed: 12-Jul-2017].

25. Engerati Blogs - Global Industry Analysis Perovskite Solar Cell Market 2016 - 2026. Available at: https://www.engerati.com/blogs/global-industry-analysis-perovskite-solar-cell- market-2016-2026.

26. “How PV Cells Work,” *How a PV System Works*. [Online]. Available: http://www.fsec.ucf.edu/en/consumer/solar_electricity/basics/how_pv_cells_work.htm. [Accessed: 16-Aug-2017].

27. “The Difference Between Solar Cell, Module and Array,” *Samlex Solar* [Online]. Available: http://www.samlexsolar.com/learning-center/solar-cell-module-array.aspx. [Accessed: 10-June-2017].

28. *PVEducation*. [Online]. Available: https://pveducation.org/. [Accessed: 09-Oct-2017].

29. Douglas, D.(2005), "Organic Photovoltaic Cells", University of Illinois.

30. “Polymer Solar Cells”, Plastic Photovoltaics [Online]. Available: http://plasticphotovoltaics.com/lc/lc- polymersolarcells/lc-how.html [Accessed: 1-June-2017].

31. G. Cotella, J. Baker, D. Worsley, F. D. Rossi, C. Pleydell-Pearce, M. Carnie, and T. Watson (2017), “One-step deposition by slot-die coating of mixed lead halide perovskite for photovoltaic applications,” *Solar Energy Materials and Solar Cells*, vol. 159, pp. 362–369.

32. M. Shirayama, M. Kato, T. Miyadera, T. Sugita, T. Fujiseki, S. Hara, H. Kadowaki, D. Murata, M. Chikamatsu, and H. Fujiwara (2016), “Degradation mechanism of CH3NH3PbI3 perovskite materials upon exposure to humid air,” *Journal of Applied Physics*, vol. 119, no. 11, p. 115501.

33. Z. Bi, Z. Liang, X. Xu, Z. Chai, H. Jin, D. Xu, J. Li, M. Li, and G. Xu (2017),“Fast preparation of uniform large grain size perovskite thin film in air condition via spray deposition method for high efficient planar solar cells,” *Solar Energy Materials and Solar Cells*, vol. 162, pp. 13–20.

34. M. K. Gangishetty, R. W. J. Scott, and T. L. Kelly (2016), "Effect of relative humidity on crystal growth, device performance and hysteresis in planar heterojunction perovskite solar cells," *Nanoscale*, vol. 8, no. 12, pp. 6300–6307.

35. L.-L. Gao, C.-X. Li, C.-J. Li, and G.-J. Yang (2017), "Large-area high-efficiency perovskite solar cells based on perovskite films dried by the multi-flow air knife method in air," Journal of Materials Chemistry A, vol. 5, no. 4, pp. 1548–1557.

36. Zhao, Y., and Zhu, K. (2014). "CH3NH3Cl-Assisted One-Step Solution Growth of CH3NH3PbI3: Structure, Charge-Carrier Dynamics, and Photovoltaic Properties of Perovskite Solar Cells." *The Journal of Physical Chemistry C*, 118(18), 9412–9418.

37. Song, X., Wang, W., Sun, P., Ma, W., and Chen, Z.-K. (2015). "Additive to regulate the perovskite crystal film growth in planar heterojunction solar cells." *Applied Physics Letters*, 106(3), 033901.

38. Okano, M., Endo, M., Wakamiya, A., Yoshita, M., Akiyama, H., and Kanemitsu, Y. (2015). "Degradation mechanism of perovskite CH3NH3PbI3 diode devices studied by electroluminescence and photoluminescence imaging spectroscopy." *Applied Physics Express*, 8(10), 102302.

39. Park, N.-G. (2015). "Perovskite solar cells: an emerging photovoltaic technology." Materials Today, 18(2), 65–72

40. Giorgi, G., and Yamashita, K. (2015). "Organic–inorganic halide perovskites: an ambipolar class of materials with enhanced photovoltaic performances." *Journal of Materials Chemistry A*, 3(17), 8981–8991.

41. Lee Seongha, 2017, "Flexible Perovskite Solar Cell On Metal Plate" M.S. thesis, Material Science, University of Pittsburgh.

42. Chen, S., Wen, X., Huang, S., Huang, F., Cheng, Y.-B., Green, M., and Ho-Baillie, A. (2016). "Light Illumination Induced Photoluminescence Enhancement and Quenching in Lead Halide Perovskite." *Solar RRL*, 1(1), 1600001.

43. Deng, X., Wen, X., Lau, C. F. J., Young, T., Yun, J., Green, M. A., Huang, S., and Ho-Baillie, A. W. Y. (2016). "Electric field induced reversible and irreversible photoluminescence responses in methylammonium lead iodide perovskite." *Journal of Materials Chemistry C*, 4(38), 9060–9068.

44. Oku, T. (2015). "Crystal Structures of CH3NH3PbI3 and Related Perovskite Compounds Used for Solar Cells." *Solar Cells - New Approaches and Reviews*.

45. Litzov, I., and Brabec, C. (2013). "Development of Efficient and Stable Inverted Bulk Heterojunction (BHJ) Solar Cells Using Different Metal Oxide Interfaces." *Materials*, 6(12), 5796–5820.

46. Yang, M., Li, Z., Reese, M. O., Reid, O. G., Kim, D. H., Siol, S., Klein, T. R., Yan, Y., Berry, J. J., Maikel F. A. M. Van Hest, and Zhu, K. (2017). "Perovskite ink with wide processing window for scalable high-efficiency solar cells." *Nature Energy*, 2(5), 17038.

47. Correa-Baena, J.-P., Abate, A., Saliba, M., Tress, W., Jacobsson, T. J., Grätzel, M., and Hagfeldt, A. (2017). "The rapid evolution of highly efficient perovskite solar cells." Energy and Environmental Science, 10(3), 710–727.

48. Maynard, B., Long, Q., Schiff, E. A., Yang, M., Zhu, K., Kottokkaran, R., Abbas, H., and Dalal, V. L. (2016). "Electron and hole drift mobility measurements on methylammonium lead iodide perovskite solar cells." *Applied Physics Letters*, 108(17), 173505.

49. Kim, J.-E., Jung, Y.-S., Heo, Y.-J., Hwang, K., Qin, T., Kim, D.-Y., and Vak, D. (2018). "Slot die coated planar perovskite solar cells via blowing and heating assisted one step deposition." *Solar Energy Materials and Solar Cells*, 179, 80–86.

50. "Perovskite solar panels developers." (n.d.). *Perovskite solar panels: introduction and market status | Perovskite-Info*, Perovskite-Info, <https://www.perovskite-info.com/companies/perovskite-solar-panels-developers> (Jun. 11, 2018).

51. "Applications – Solar." (n.d.). *Applications – Solar |*, <http://gr2l.co.uk/applications-solar/> (Aug. 12, 2017).

52. "REC Silicon-Technology", G*lossary*|<https://www.recsilicon.com/technology/glossary>(March 8, 2018)

53. "Spin Coating: A Guide to Theory and Techniques", Ossila [Online]" |, <https://www.ossila.com/pages/spin-coating. [Accessed: 02- May- 2017].

54. Hoth, C. N., Schilinsky, P., Choulis, S. A., Balasubramanian, S., and Brabec,C. J., September 2012, "Solution-Processed Organic Photovoltaics, Applications of Organic and Printed Electronics" Springer Science and Business Media, pp. 27–56]

55. He, M., Li, B., Cui, X., Jiang, B., He, Y., Chen, Y., O'Neil, D., Szymanski, P., Ei-Sayed, M. A., Huang, J., and Lin, Z. (2017). "Meniscus-assisted solution printing of large-grained perovskite films for high-efficiency solar cells." *Nature Communications*, 8, 16045.

56. Hwang, K., Jung, Y.-S., Heo, Y.-J., Scholes, F. H., Watkins, S. E., Subbiah, J., Jones, D. J., Kim, D.-Y., and Vak, D. (2015). "Toward Large Scale Roll-to-Roll Production of Fully Printed Perovskite Solar Cells." *Advanced Materials*, 27(7), 1241–1247.

57. Krebs, F. C. (2009). "Fabrication and processing of polymer solar cells: A review of printing and coating techniques." *Solar Energy Materials and Solar Cells*, 93(4), 394–412.

58. Exair, C., 2017, "Standard Air-Knives catalogue"

59. Adam, G., Kaltenbrunner, M., Głowacki, E. D., Apaydin, D. H., White, M. S., Heilbrunner, H., Tombe, S., Stadler, P., Ernecker, B., Klampfl, C. W., Sariciftci, N. S., and Scharber, M. C. (2016). "Solution processed perovskite solar cells using highly conductive PEDOT:PSS interfacial layer." *Solar Energy Materials and Solar Cells*, 157, 318–325.

60. Liu, Z., Zhu, A., Cai, F., Tao, L., Zhou, Y., Zhao, Z., Chen, Q., Cheng, Y.-B., and Zhou, H. (2017). "Nickel oxide nanoparticles for efficient hole transport in p-i-n and n-i-p perovskite solar cells." *Journal of Materials Chemistry A*, 5(14), 6597–6605.

61. Franeker, J. J. V., Hendriks, K. H., Bruijnaers, B. J., Verhoeven, M. W. G. M., Wienk, M. M., and Janssen, R. A. J. (2016). "Monitoring Thermal Annealing of Perovskite Solar Cells with In Situ Photoluminescence." *Advanced Energy Materials*, 7(7), 1601822.

62. Simões, A., González, A., Zaghete, M., Varela, J., and Stojanovic, B. (2001). "Effects of annealing on the crystallization and roughness of PLZT thin films." *Thin Solid Films*, 384(1), 132–137.

63. Ren, X., Yang, Z., Yang, D., Zhang, X., Cui, D., Liu, Y., Wei, Q., Fan, H., and Liu, S. (F. (2016). "Modulating crystal grain size and optoelectronic properties of perovskite films for solar cells by reaction temperature." *Nanoscale*, 8(6), 3816–3822.

64. Zhu, L., Shi, J., Lv, S., Yang, Y., Xu, X., Xu, Y., Xiao, J., Wu, H., Luo, Y., Li, D., and Meng, Q. (2015). "Temperature-assisted controlling morphology and charge transport property for highly efficient perovskite solar cells." *Nano Energy*, 15, 540–548.

65. Huang, Y.-C., Tsao, C.-S., Cho, Y.-J., Chen, K.-C., Chiang, K.-M., Hsiao, S.-Y., Chen, C.-W., Su, C.-J., Jeng, U.-S., and Lin, H.-W. (2015). "Insight into Evolution, Processing and Performance of Multi-length-scale Structures in Planar Heterojunction Perovskite Solar Cells." *Scientific Reports*, 5(1).

66. Paek, S., Schouwink, P., Athanasopoulou, E. N., Cho, K. T., Grancini, G., Lee, Y., Zhang, Y., Stellacci, F., Nazeeruddin, M. K., and Gao, P. (2017). "From Nano- to Micrometer Scale: The Role of Antisolvent Treatment on High Performance Perovskite Solar Cells." *Chemistry of Materials*, 29(8), 3490–3498.

67. Seth, S., and Samanta, A. (2017). "Photoluminescence of Zero-Dimensional Perovskites and Perovskite-Related Materials." *The Journal of Physical Chemistry Letters*, 9(1), 176–183.

68. Zhang, B., Guo, F., Xue, J., Yang, L., Zhao, Y., Ge, M., Cai, Q., Liu, B., Xie, Z., Chen, D., Lu, H., Zhang, R., and Zheng, Y. (2017). "Photoluminescence Study of the Photoinduced Phase Separation in Mixed-Halide Hybrid Perovskite CH3NH3Pb(BrxI1−x)3 Crystals Synthesized via a Solvothermal Method." *Scientific Reports*, 7(1).

69. Tzounis, L., Stergiopoulos, T., Zachariadis, A., Gravalidis, C., Laskarakis, A., and Logothetidis, S. (2017). "Perovskite solar cells from small scale spin coating process towards roll-to-roll printing: Optical and Morphological studies." *Materials Today: Proceedings*, 4(4), 5082–5089.

Appendix

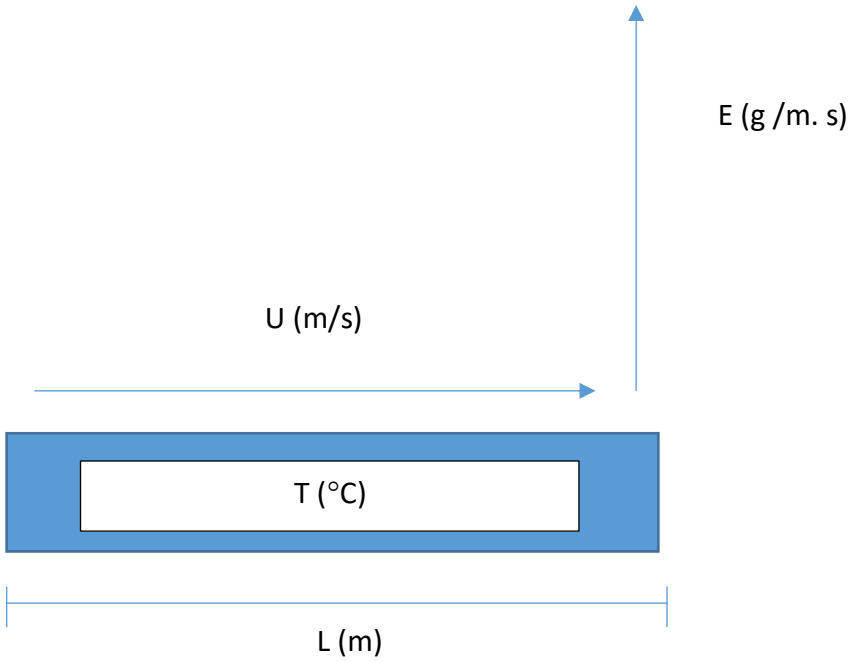

Fig. 1 Flat plate evaporation model

Reynolds Number (*Re*) $\frac{UL}{\nu}$

Schmidt Number (*Sc*) $\frac{\nu}{D}$

Sherwood Number (*Sh*) $\frac{kL}{D}$

$Sh = 0.664(Re^{0.5}Sc^{0.333})$

[*U*=air velocity (20.3 *m/s*); *L*=length of the plate (0.1 *m*); ν= kinematic viscosity of air (22.8*10^{-6} m^2/s); *D*= diffusion coefficient of the solvent in air (8.28*10^{-2} m^2/s); *k*=mass transfer coefficient (*m/s*)]
Sh=12.924; *k*=10.714 *m/s*
c = VP/RT [R=8.314 *J/mol. K, T*=368 *K]*

log (VP) = AA-AB/(AC+T) [AA=3.9306*; AB*=1337.716*; AC*=-82.648*; T*=368 *K,* *VP*=Vapour Pressure]
VP=0.174 *bar; c*=5.53*10^{-3} *mol/L*
$E = kLc$ [*k*=10.714 *m/s L*= 0.1 *m*; *c*=5.53*10^{-1} g /cm^3]
E=0.59248 *g/m. s*
$\rho = m/V$
Volume of DMF solvent evaporated from the bed of the r & d sheet coater from the coated film in the presence of N_2*= 0.59606 ml/m. s*

Design diagrams

1. Prototype chamber

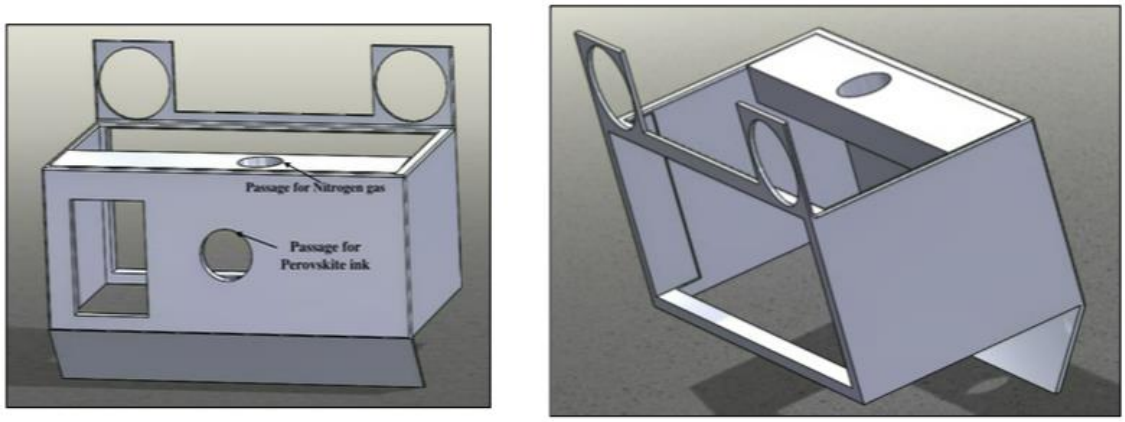

Fig. 2 Prototype chamber designs

2. Large-area chamber

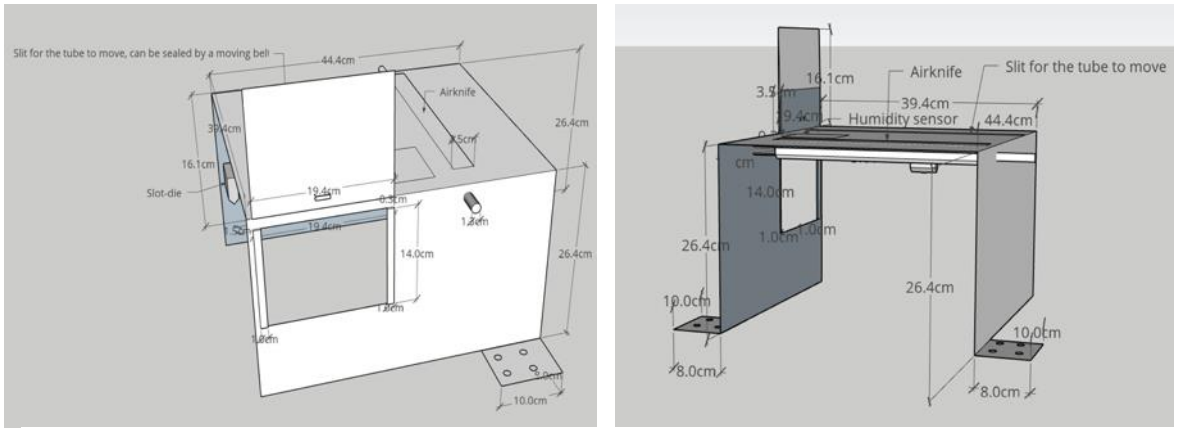

Fig. 3 Large-area chamber designs on SketchUp Pro 2018

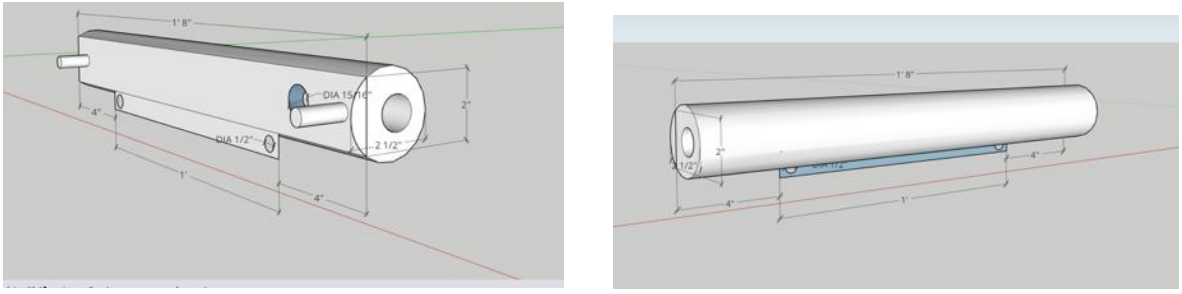

Fig. 4 Design of the air-knife mounting tube

ANSYS simulation

Version	Release 18.1
Solver	Pressure-Based
Turbulence Model	k-epsilon (2 equation)
Order of equations used	**Pressure**: Second Order **Momentum**: Second Order Upwind **Turbulent Kinetic Energy**: First Order Upwind **Turbulent Dissipation Rate**: First Order Upwind **Energy**: Second Order Upwind
Number of elements in mesh	63270; **Element type**: Quadrilateral dominant
Boundary conditions	**Pressure inlet**: (Gauge) 103421 Pa **Pressure outlet**: (Gauge) 0 Pa **Heated deposition bed temperature**: 368K No-slip condition

Table 8 CFD modeling simulation parameters

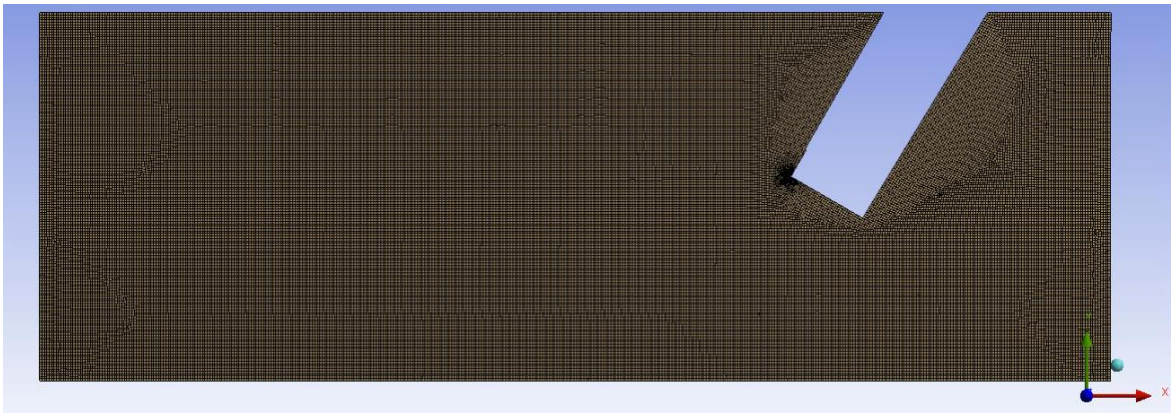

Fig. 5 A generated mesh for the large-area chamber

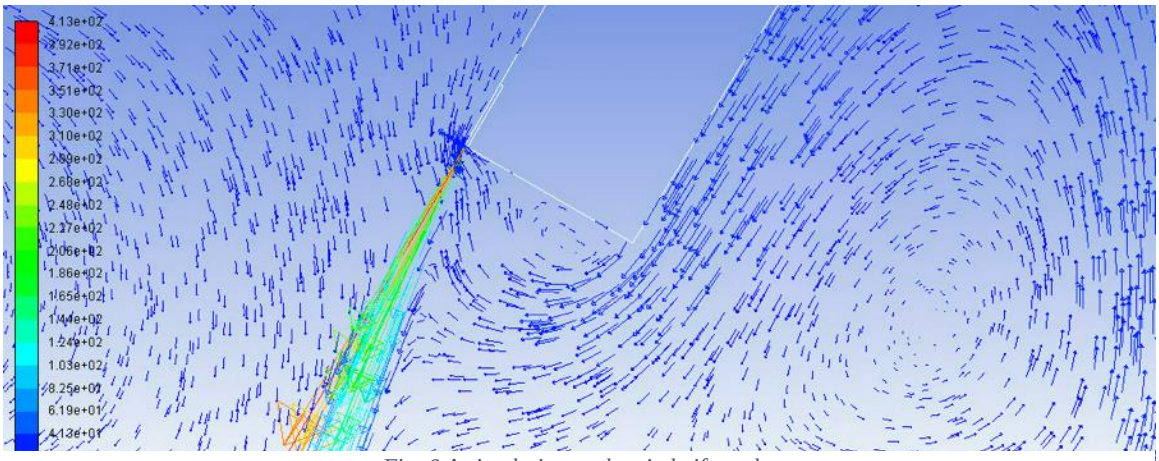

Fig. 6 A simulation at the air-knife outlet

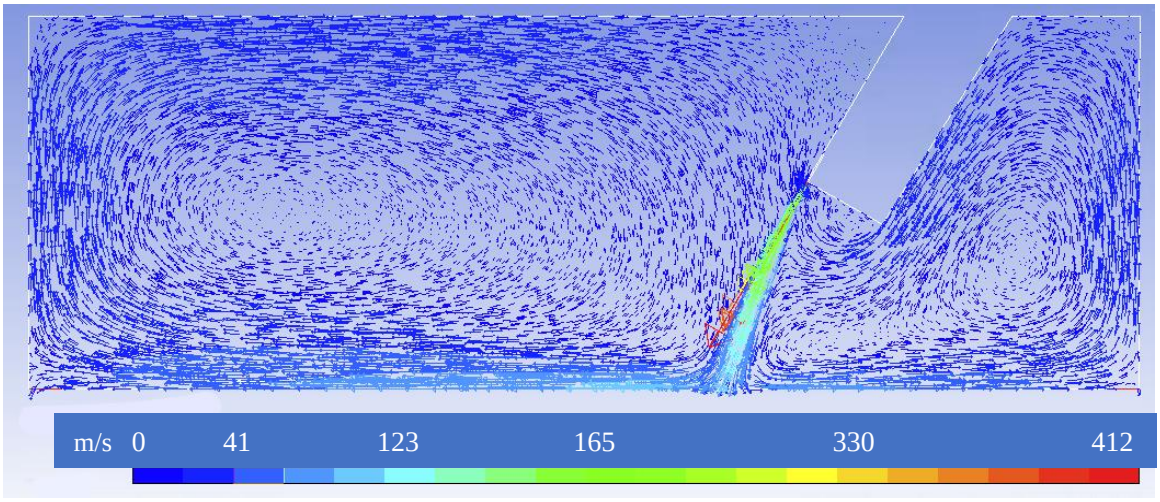

Fig. 7 A simulation of the entire chamber

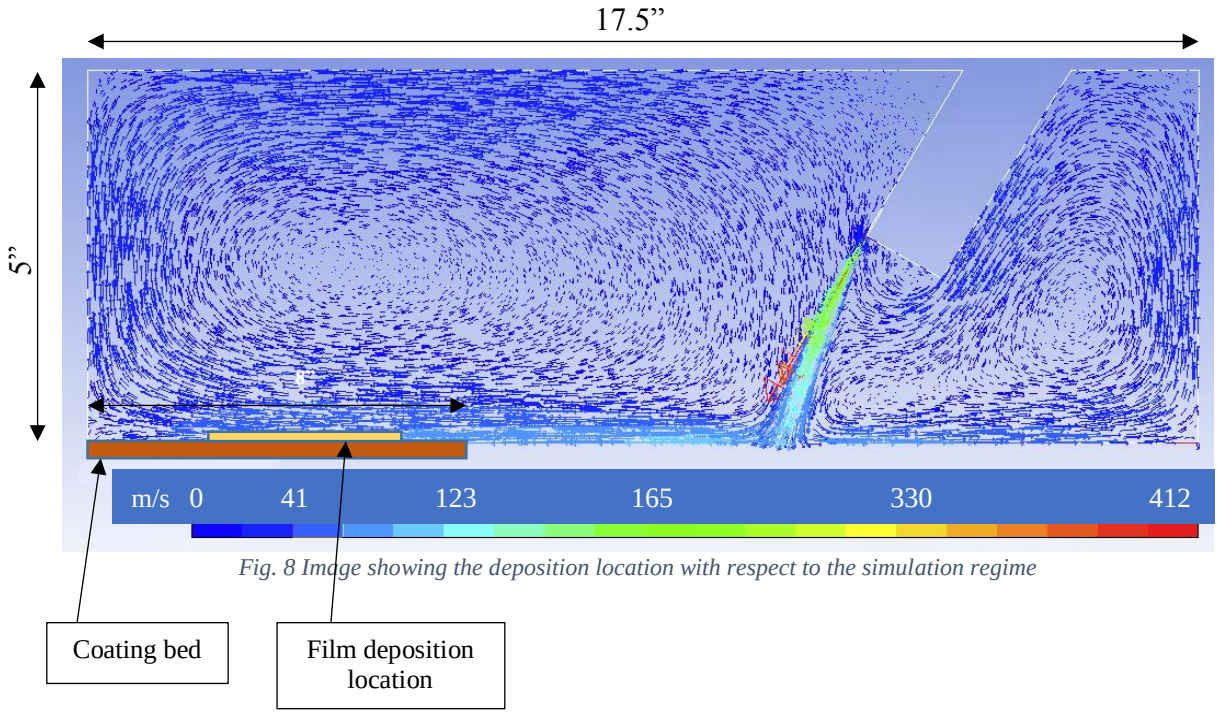

Fig. 8 Image showing the deposition location with respect to the simulation regime